Multi-scale Deformation and Failure Prediction of Polycrystalline Metals: A Case Study on Impact and Localization

by

Morad Mirzajanzadeh

A Dissertation Submitted to the
Graduate School of Science and Engineering
in Partial Fulfillment of the Requirements for
the Degree of

Master of Science

in

Mechanical Engineering

KOÇ
UNIVERSITY

September 21, 2016

Multi-scale Deformation and Failure Prediction of Polycrystalline Metals: A Case Study on Impact and Localization

Koç University

Graduate School of Sciences and Engineering

This is to certify that I have examined this copy of a master's thesis by

Morad Mirzajanzadeh

and have found that it is complete and satisfactory in all respects,

and that any and all revisions required by the final

examining committee have been made.

Committee Members:

_____

Assoc. Prof. Demircan Canadinç

_____

Assoc. Prof. B. Erdem Alaca

_____

Prof. Thomas Niendorf

Date: _____

I would like to dedicate this thesis to my life mentor, best friend and supervisor Assoc. Prof. DEMİRCAN CANADİNÇ

ABSTRACT

The widespread use of polycrystalline materials in advanced and infrastructural technologies demands a proper understanding of the mechanical response at multiple length scales. Today's high demand to foster higher speeds in public transportation media has introduced the need for designing new materials that can be safely employed under severe loading conditions, in addition to being impact-tolerant. Furthermore, ductile fracture of polycrystalline metals commonly ensue plastic flow localization through the mechanisms involving void nucleation, growth and coalescence. As a precursor of failure and a limit that mark uniform straining of ductile metallic materials, detection of the localization is highly crucial. In order to investigate multiscale impact and failure response of the polycrystalline metallic materials two case studies were considered here. In the first part a microstructural-sensitive simulation of the high-manganese austenitic steel under impact loading was performed. Next, using in-situ SEM tests of AISI 316L stainless steel macroscopic plastic localization was investigated.

In part (I) microstructurally-informed macroscopic impact response of a high-manganese austenitic steel was modeled through incorporation of the visco-plastic self-consistent (VPSC) crystal plasticity model into the ANSYS LS-DYNA non-linear explicit finite element (FE) code. Voce hardening flow rule was utilized in the VPSC crystal plasticity model to predict the micro-mechanical response of the material, which was calibrated based on experimentally measured quasi-static uniaxial tensile deformation response and initially measured textures. Specifically, hiring calibrated Voce parameters in VPSC, a modified material response was predicted employing local velocity gradient tensors obtained from the

initial FE analyses as a new boundary condition for loading state. The updated micro-mechanical response of the material was then integrated into the macro-scale material model by calibrating the Johnson-Cook (JC) constitutive relationship and the corresponding damage parameters. Consequently, we demonstrate the role of geometrically necessary multi-axial stress state for proper modeling of the impact response of polycrystalline metals, and validate the presented approach by experimentally and numerically analyzing the deformation response of the Hadfield steel under impact loading.

In part (II) of this study, plastic localization was investigated by tracking the captured incremental images during the micro scale in-situ scanning electron microscope (SEM) tensile experiment of samples made from AISI 316L stainless steel. A novel hybrid-numerical experimental (HNE) approach for small scale tensile testing of materials is developed. An unconventional miniaturized test set-up was designed to reach smaller scales in testing and also to eliminate displacement errors due to vertical spatial distortion during the in-situ SEM measurements. By arranging each pair of sequentially taken surface images – over deformation history – in alternate order for several repetition, plastic localization regions became manifest on surface. Results clearly prove feasibility of the presented method in recording primary plastic localization events within an in-situ SEM tensile testing framework.

ÖZETÇE

Polikristal malzemelerin temel ve ileri teknoloji alanlarında yaygın kullanılması için bu malzemelerin mekanik davranışlarının farklı ölçeklerde anlamlandırılması gerekmektedir. Toplu ulaşım araçlarının daha yüksek hızlarda hizmet verebilmesi için malzemelerin sert koşullara ve darbelere dayanıklı, yüksek güvenlikli yeni malzemelerin tasarımına ihtiyaç duyulmaktadır. Buna ek olarak, polikristal metallerin sünek kırılması plastik akış lokalizasyondan sonra başlamaktadır. Lokalizasyon mekanizmaları, malzemedeki boşlukların başlaması, büyümesi ve birleşmesi olaylarını içerir. Tipik olarak, lokalizasyonun kırılmadan önce meydana gelmekte ve sünek metalik malzemelerdeki tekdüze bir gerinimi sınırlandırmaktadır. Polikristal metalik malzemelerin farklı ölçeklerdeki darbe ve kırılma davranışlarını incelemek için iki vaka çalışması yapılmıştır. Birinci kısımda, yüksek-manganez östenitik çeliğin darbe yükü altındaki durumu mikroyapı-eksenli simülasyon ile analiz edilmiştir. Daha sonra, AISI 316L paslanmaz çeliğin in-situ SEM (taramalı elektron mikroskopu) testleri yardımıyla makroskobik plastik lokalizasyonu incelenmiştir.

Birinci kısımda, yüksek-manganez östenitik çeliğin mikroyapı-eksenli makroskobik darbe davranışı ANSYS LS-DYNA doğrusal olmayan explicit sınırlı eleman (FE) kodu içerisine VPSC (visco-plastik self-consistent) kristal plastik modeli eklenerek modellenmiştir. Malzemelerin mikro-mekanik davranışlarını tahmin etmek için VPSC kristal plastik modelinde Voce sertleşmesi akış kuralları kullanılmıştır. Bu akış modeli tek eksenli statik çekme test sonuçları ve malzemenin başlangıç mikroyapı bilgileriyle kalibre edilmiştir. Özellikle, VPSC'deki kalibre edilmiş Voce parametreleri yardımıyla, yerel hız gradyant tansörü yeni sınır koşulları gibi kullanılarak modifiye edilmiş malzeme davranışları tahmin edilmiştir. Bu yararlanılan yerel hız gradyant tansörü başlangıçtaki FE analizlerinden elde

edilmiştir. Malzemelerin güncellenmiş mikro-mekanik davranışları Johnson-Cook (JC) bünye ilişkisi ve eşlenik hasar parametreleri ile kalibre edilerek makro-yapı malzeme modeline entegre edilmiştir. Sonuç olarak, polikristal malzemelerin darbe davranışlarına uygun bir modellemenin yapılabilmesi için geometriye bağlı çok eksenli gerilim durumun (stress state) gerekliliğini ortaya çıkarılmıştır. Ayrıca, bahsi geçen metodun Hadfield çeliğinde darbe sonucu oluşan deformasyon davranışının deneysel ve numerik olarak analizinde kullanılabileceğini gösterdik.

İkinci kısımda, AISI 316L paslanmaz çelikten yapılan numunelerin mikro ölçek in-situ SEM çekme testinde kaydedilen sıralı görüntülerini kullanarak plastik lokalizasyonunu inceledik. Küçük ölçekteki malzemelerin çekme testi için yeni bir yaklaşım olan HNE'yi (hybrid-numerical experimental) geliştirdik. Bu yaklaşım çerçevesinde, daha küçük ölçeklerde test yapabilmek ve in-situ SEM ölçümlerindeki yatay mekânsal yamulmanın oluşturduğu deplasman hatalarını azaltmak için çekme düzeneği özgün bir şekilde minyaturlaştırıldı. Numune deformasyon sırasında art arda çekilmiş iki görüntü daha sonra birkaç kez kopyalanıp tekrarlanarak dizi haline getirildi. Oluşturulan görüntü dizisi yardımıyla plastik lokalizasyon bölgeleri ortaya çıkarıldı. In-situ SEM çekme testlerinden elde edilen sonuçlar, geliştirdiğimiz metodun öncül plastik lokalizasyonu saptamada kullanılabileceğini kanıtlamaktadır.

ACKNOWLEDGMENTS

Here, I would like to express my special appreciation and thanks to my advisor Assoc. Prof. DEMİRCAN CANADİNÇ, you have been an excellent mentor for my study and life. I would like to thank you for encouraging my research and for allowing me to grow as an independent research scientist in this fascinating area. Your advice on both my research and future career has been priceless. I would also like to thank my committee members, Prof. THOMAS NIENDORF, Assoc. Prof. B ERDEM ALACA for serving as my committee members. I would like to show my gratitude to all the staff in the Engineering Department at Koc University and Institute of Materials Engineering at Technische Universität Bergakademie Freiberg. I would like also to highly appreciate the received support from Prof. THOMAS NIENDORF and Dr. ANJA WEIDNER during my visiting stay in Freiberg. All of you have been there to support me when I need any type of support for my research and study.

A special thanks to my family. Words cannot express how grateful I am to my mother-in law, father-in-law, my mother, and father, my sisters and brothers-in-law for all of the sacrifices that you have made on my behalf. Your prayer for me was what sustained me this far. I would also like to thank all of my friends who supported me in writing, and motivated me to strive towards my goals. At the end, I would like express appreciation to my beloved wife ELMIRA REZAEI SEPASI who spent sleepless nights with me and was always my support in the moments when there was no one there.

I would also like to greatly thank my dear officemates, BERKAY GUMUS, BURAK BAL, BENAY UZER, CEMRE OZMANCI, MINE TOKER and ORKUN ONAL at Advanced Materials Group (AMG) at Koc University for their never-ending friendly support and making unforgettable moments during my stay in Turkey, and DOMINIK KREWERTH,

JOHANNES SOLAREK and MALTE VOLLMER for their great support during my three months visiting period at Institute of Materials Engineering at Technische Universität Bergakademie Freiberg. Here, I would also like to highly appreciate priceless help and support of my great friend BEKIR AKSOY for motivating me during my study and also his precious favor for writing the *ÖZETÇE*.

Finally, I would like to express my special gratitude and appreciation to my dear nephew, ELYAR ESMAEILZADEH for his invaluable support and kind help in writing and preparing this thesis.

TABLE OF CONTENTS

page

LIST OF TABLES

page

LIST OF FIGURES

page

LIST OF SUPPLEMENTERY MATERIALS page

Chapter 1

INTRODUCTION

1.1. PREVIEW

The present chapter introduces the motivation and significance of the current work. This research is divided into two separate case studies on impact and localization of polycrystalline metallic materials. Details of the literature background for this study will be dealt with in Chapter 2 and 3 specifically.

1.2. MOTIVATION AND SIGNIFICANCE

The first part of this study is an attempt to establish a methodology to predict the macroscopic impact response of polycrystalline metals by properly treating the microstructural features and their influence on the deformation response, in addition to improving our understanding of the physics and mechanics of high-velocity loading. It is well known that the deformation of a polycrystalline aggregate is dictated by the activities and interactions of micro-deformation mechanisms regardless of the applied macroscopic stress state, and thus, one can argue that the proper modeling of the micro-deformation of a material even under the simplest loading scenario will lead to an accurate prediction of the deformation response under any combination of applied loading. However, a simple continuum model capable of taking into account the microstructure for predicting the impact response has not been forwarded yet. In order to address this issue, we propose a multi-scale model to simulate microstructurally-informed macroscopic impact response of polycrystalline metallic

materials, which also offers a great potential for industrial applications owing to its practicality. Specifically, coupling of VPSC with FE allowed for capturing the roles of anisotropy induced by plastic deformation and geometry, and micro-deformation mechanisms throughout the complicated impact deformation.

Difficulties involved in practical testing of materials under impact loading and intrinsic restrictions brought about by the test of complex structures demands a substitute model for prediction of material behavior under the action of high-velocity loads. Additionally, it is sometimes a prerequisite of a design to comprehend the impact response of a newly engineered material in order to get further information on material itself or improve its microstructure to tailor its mechanical properties. Even though there is wealth of information about the significance of microstructural features in accurate prediction of deformation response, a tangible scarcity of models that are capable of consider multi-scale mechanics of material during impact loading in a continuum sense still exists. The proposed modeling approach in this study not only confirms the significant role of microstructure in accurate modeling of macro-scale response of austenitic high-manganese steels, but it also introduces a methodology through which prediction of the material response during impact loading can be readily achieved. In fact, combination of the microstructural evolution and deformation rate in modeling leads to high-accuracy predictions, where stress multi-axiality, complex geometry and rate dependency of the material were all considered. Overall, the presented research illuminates the next step towards improved prediction of the macroscopic response of polycrystalline solids under high-velocity loading.

The second part of this research was designed to invent small-scale testing methodology for observation of macroscopic plastic localization as the precursor to ductile fracture in polycrystalline metallic materials. While there are plenty of the numerical/theoretical studies on localization mechanisms such as void nucleation, growth and coalescence, experimental

investigations in this field are scarce. This is mainly due to the involved difficulty in observation of damage nucleation and growth inside the metallic materials and their unpredictable locations. As a precursor of failure and a limit that mark uniform straining of ductile metallic materials, detection of the localization is highly crucial in different fields such as metal forming. This work will introduce a novel simple experimental approach for finding the uniform straining limit of ductile metals. Finally, it is shown that observation of the macroscopic localization events become possible using the presented testing method in an inexpensive fashion.

Chapter 2

A MICROSTRUCTURE-SENSETIVE SIMULATION OF IMPACT RESPONSE IN A HIGH-MANGANESE AUSTENITIC STEEL

2.1. INTRODUCTION

The widespread use of polycrystalline materials, such as high-manganese austenitic steels, in high-speed transportation media demands a proper understanding of the mechanical response under severe loading conditions, for instance impact. Accuracy and reliability in impact design is very crucial since the imposed damage is mostly significant, costly and may even result in severe loss of life or property. However, when materials are subjected to impact loading, they are significantly affected by large deformations, high strain rates, temperature softening, varying stress states, as well as loading history, which cause damage nucleation, propagation, and eventually failure [1,2]. Each of the aforementioned key aspects needs proper investigation in design, as the final response of the structure will be affected by all these factors, as well as inter-correlation properties. In polycrystalline materials, such as Hadfield steel (HS), a special load-bearing class of high-manganese austenitic steels, the micro-scale deformation mechanisms and plastic anisotropy due to inhomogeneous texture have also a noticeable effect on general macroscopic behavior of the media, and require a detailed treatment [3-6]. A good example of this has been studied on a wrought magnesium alloy subjected to high strain rate loading which shows significant dependency on texture [7]. Another representative case can be found in an experimental investigation into micro-deformation mechanisms of Hadfield steel under impact loading [8].

There are myriad of studies that proposed or modified constitutive equations to model the deformation response of materials exposed to high strain rates and elevated temperatures [9-17]. Gurson in 1977 [10], and Johnson and Cook six years later [11], proposed the most prevalent ductile damage models of the present time, which successfully simulate deformations in high strain rate loading regimes. Combination of these methods with other criteria, and their modification or validation, has attracted a great deal of attention over the years [18-20]. In particular, it is much easier to derive JC model parameters as compared to those of other sophisticated constitutive relations [14], such as Zerilli-Armstrong (ZA) [12]. Specifically, the JC model was demonstrated to suitably include stress triaxiality in tensile loading/failure mode and strain rate effects in steel, thereby providing good estimations of high-velocity impact loading response and ductile damage evolution [21, 22].

Even though many of the previous works do not explicitly report the effect of strain rate on *fracture strain vs. stress triaxiality relation*, their results indicate substantial attenuation in dependency of fracture strain on stress triaxiality under dynamic loading [21, 23]. In contrast, it was shown that the ductile fracture strain is strongly dependent on the stress triaxiality under quasi-static loading conditions [24]. Bao and Wierzbicki [25] showed that a single criterion is insufficient to capture all features of ductile crack formation under different stress states and proposed a novel ductile fracture curve in the equivalent strain and stress triaxiality space.

In addition to the unquestionable difficulties involved in deriving the material and damage constants of the proposed damage and material relationships, the finite element (FE) simulation of Charpy impact test has its own complexity. For instance, reported FE simulations of the Charpy impact test [26-28] suffer from two shortfalls: the material response at the onset of deformation is usually overestimated, and/or the softening observed during impact is generally underestimated.

Yet, to the best of the authors' knowledge, none of the aforementioned models and other studies available in the literature take the effects of microstructural features and micro-deformation mechanisms into account in predictions of macro-scale impact response. Even though multi-scale modeling techniques, such as crystal plasticity finite element (CPFE) and molecular dynamics (MD) are increasingly applied to include microstructural features in simulations [29-31], the associated computational costs and involved complexities in such methods are patent. The convolution and low efficiency of the new developments in the field of micro-deformation modeling and molecular dynamics, and the incorporation of these models into FE software make them quite inapplicable to industrial problems and impose hefty expenses, and thus, their execution by industry is still controversial. Yet these powerful methods can successfully be employed as validation tools for proposed macroscopic constitutive relationships. On the other hand, although conventional constitutive material models implemented in available FE packages can predict the macroscopic response of a material, they mostly fail to apprehend the associated micro-deformation mechanisms, and therefore, they are unable to predict the deformation response of materials with complex microstructure [31].

In this study, microstructure-dependent macroscopic impact response of HS was simulated through incorporation of a visco-plastic self-consistent (VPSC) crystal plasticity model into a macro-scale FE model. The initial FE modeling was performed employing experimentally recorded quasi-static uniaxial tensile test data via ANSYS software with explicit LS-DYNA solver [32]. The same test data was utilized to incorporate the roles of experimentally measured microstructural features, including texture and active micro-deformation mechanisms, into the VPSC algorithm to model the micro-deformation behavior of polycrystalline aggregate on selected material domains. To do so, the micro-deformation response of the material was calibrated using the Voce hardening flow rule. Then, the

obtained velocity gradient of the primarily solved FE model was introduced to the calibrated VPSC algorithm as an updated boundary condition. Thereby, microstructural response of the polycrystalline aggregate was estimated in the presence of multi-axial loading state. Modified material responses of the selected domains were then averaged and eventually employed in the updated macroscopic FE model through JC constitutive relation. To consider the strain rate effects and to attribute ductile damage mechanisms, JC material and damage models were employed and initially calibrated based on the available experimental data on HS in the literature and quasi-static uniaxial tensile deformation data.

2.2. MICROSTRUCTURAL EFFECTS AND DUCTILE FRACTURE

Texture-based anisotropy (or plastic anisotropy) plays a key role in the micro deformation, surface topography, and eventually general deformation response of polycrystalline materials. Additionally, micro-deformation mechanisms are reported [31] to constitute one of the pivotal factors dictating the macroscopic response of metals with high degree of anisotropy, such as high-manganese austenitic steels. Nevertheless, implementation of multi-scale modeling techniques which are capable of taking these factors into account require subsequent homogenization techniques and are very costly: they need highly technical and advanced equipment, and rigorous scientific considerations, which makes them undesirable in industry. Hence the lack of a simple microstructure-sensitive model capable of predicting high strain rate deformation response, such as the impact response, of polycrystalline materials is largely felt.

From a macroscopic point of view, stress triaxiality and strain rate have an important role on the deformation response of metallic materials. The literature offers various studies about stress triaxiality effects on ductile fracture [21, 23, 24], through which a clear account for the

comprehension of such effects has been delivered. To derive this relationship, one should find equivalent failure strain ($\bar{\varepsilon_f}$) of the material for different loading condition, i.e. under tensile (region R1), shear (region R2) and compression (region R3) loads which will result in a spectrum of average stress triaxiality $\eta = \left(\frac{\sigma_H}{\bar{\sigma}}\right)_{av}$ as shown in Fig. 2.1. In stress triaxiality equation, σ_H is the hydrostatic stress and $\bar{\sigma}$ is von Mises flow stress. This graph depicts a schematic distribution of the fracture strain over a possible range of stress triaxiality and hypothetical effect of strain rate on this relationship. Represented schematic JC damage models in Fig. 2.1 are modified with respect to a cut-off value for the negative triaxiality for fracture [33] and specific loading condition for the Charpy impact test.[1] Accordingly, it was concluded that there was a possible slope discontinuity in the fracture locus corresponding to the point of fracture mode transition [24]. Yet this behavior is very complicated and varies significantly in different materials; furthermore, it needs a rage of tests to draw a similar graph for each strain rate level. While various investigations have been carried out on the stress triaxiality in low strain rate loading, there is no solid understanding on the effect of strain rate on stress triaxiality. Nevertheless, latest research demonstrates that the change in failure strain due to geometrical features at higher strain rates was by far smaller as compared to their lower strain rate counterparts [21, 34].

[1] The corresponding details are provided in *Section 3*.

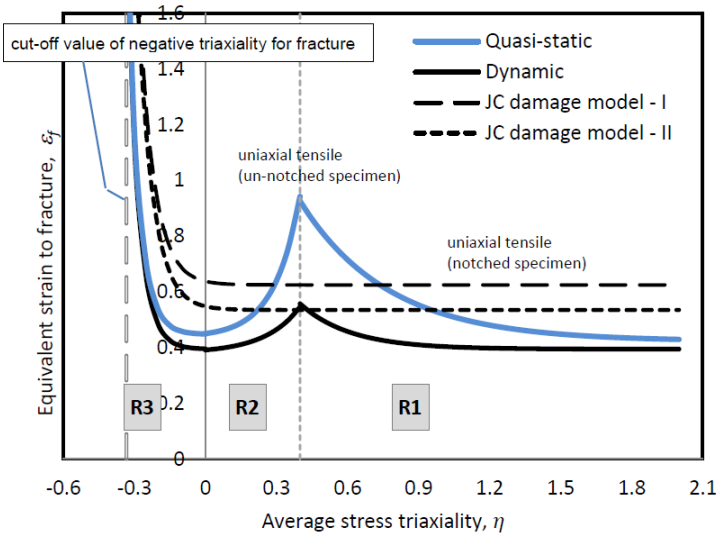

Fig. 2.1. Schematic illustration of the dependency of equivalent strain to fracture on the stress triaxiality in polycrystalline metals and the JC damage model (I and II represent different strain rates) modified with respect to the cut-off value of negative triaxiality for fracture.

Considering the relatively inconsequential effect of stress triaxiality on failure strain in steels at higher strain rates based on previous reports, and in order to avoid the difficulty involved in its experimental measurement, in this work we assume that the failure strain of HS at high strain rates (higher than 3000 s^{-1}) is independent of the stress triaxiality over the R1 and R2 regions. Consequently, for the entire R1 and R2 ranges, a plateau shaped *equivalent plastic failure – stress triaxiality* $(\bar{\varepsilon}_f - \eta)$ behavior with magnitude of the failure strain of uniaxial tensile specimens in the given strain rates is assumed. The $(\bar{\varepsilon}_f - \eta)$ behavior within the R3 region will be explored in detail in the remainder of this paper in accord with the JC damage model.

2.3. MATERIAL DESCRIPTION

2.3.1. Experimental procedure

V-notch Charpy specimens extracted from a HS slab containing 12.4 wt. % manganese and 1.1 wt. % carbon were investigated under impact loading. Impact samples with dimensions of 2.8 mm × 4 mm × 25 mm, including a notch with a radius of 0.1 mm, a 60-degree notch angle and a notch depth of 1 mm were utilized (Fig. 2.2). Impact specimens were cut from bulk via electro-discharge machining (EDM) technique. Test samples were crashed by the Charpy impact test hammer (striker) with the energy of 50 J and maximum initial velocity of 3.8 m/s, and the data were recorded at a frequency of 2 MHz. Strain gauge on the hammer peen detected the forces during the experiment, and a displacement sensor was employed to establish the position and speed of the hammer at each time interval. Another set of impact samples were heated to three different temperatures prior to testing.

Fig. 2.3 depicts force vs. time results obtained from three similar tests performed at 323 K (Fig. 2.3a) and another set of experiments carried out at four different temperatures (Fig. 2.3b). Oscillations at the beginning of the experiment are due to the strong bending mode that will be quickly damped by plasticity [27]. It is apparent in Fig. 2.3b that the impact response of HS shows a little material softening at elevated temperatures. As Fig. 2.3a reveals, increase in force continues up to about t=1.2 ms (t measured from the beginning of the impact: *deformation time = 0.25ms* in Fig. 2.3), and then the force slightly decreases for about t=0.2 ms before exhibiting a steep decrease over the final part of the loading which lasts for approximately t=2 ms. This behavior can be reasoned based on the damage origination and progression, which is synchronized by the material hardening over the span of the high-speed loading. When the competition between damage weakening and material hardening is won by the ductile crack propagation (at about t=1.2 ms: where the slope of the graph equals zero), the material hardening rate is not enough to compensate this loss of the material ligament, such that the material rapidly loses its stiffness, eventually giving way to the failure of the whole specimen.

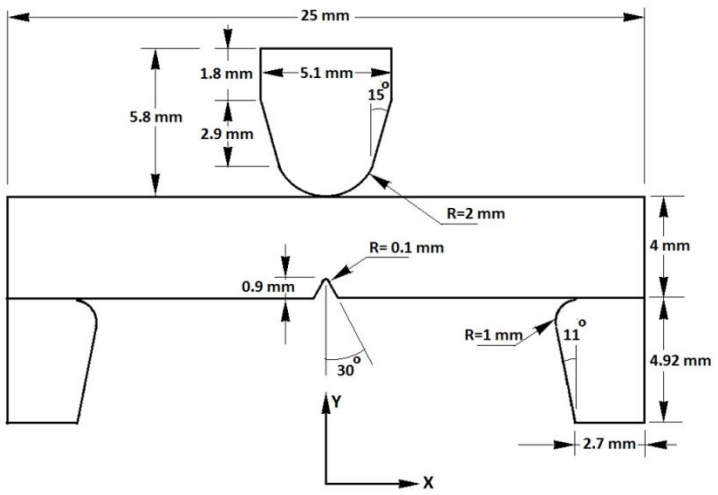

Fig. 2.2. Dimensions of impact specimens (utilized in the experiments) besides geometry of the fixed supports (beds) and hammer employed in the FE simulation.

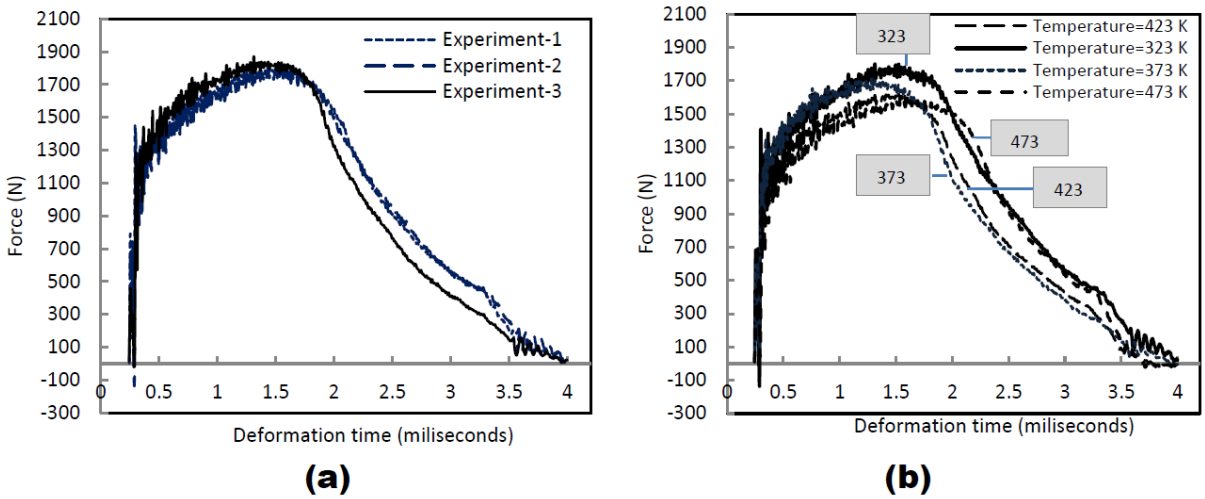

Fig. 2.3. Experimental impact test results: (a) force vs. time in temperature of 323 K using three similar specimens of HS, and (b) force vs. time using four differently heated HS specimens.

In order to obtain information about the initial microstructures and the corresponding initial textures for the subsequent numerical analysis and post-impact analysis, the notch tips and middle part of specimens were examined through X-ray diffraction (XRD) and scanning electron microscopy (SEM) techniques. SEM results in Fig. 2.4 illustrate fracture regions in

the vicinity of the crack tip for a sample deformed at 473 K. Extremely protruded edges in the middle part of the specimen on the hammer-impacted side due to the large compressive loads are evident in Fig. 2.4a. Initiated or trapped micro-cracks along the grain boundaries and regions with dense slip activities are also identified in Fig. 2.4b. Highly twinned areas around the cracked region were reported also in [35], but twinning is not considered in the current simulations for the sake of simplicity. Additionally, this image clearly ascertains the role that microstructural features and micro-deformation mechanisms have on macroscopic deformation through the left-behind uneven surface of the specimen, specifically around the crack evolution path. Vicinity of the crack growth path is clearly dominated by a copious volume of slip lines and extruded zones due to intense slip activity with a high concentration around the crack edge, while their intensity fades away on the regions far from the crack edge (see Fig. 2.4c and d). Specifically, areas around the crack path is fully occupied by the severe dislocation activities. This can be tracked by focusing on the slip lines and very uneven final surface which is a direct result of the microstructure and crystal-level deformation activities. When majority of this large permanent deformation is accommodated by slip (and twinning, though were not included in the current study), then considering a suitable crystal plasticity (microstructural) model should yield a more accurate prediction of the flow rule, hardening behavior, and final stress state. The effect of microstructure is negligible in isotropic polycrystalline materials whereas these become more pronounced in metals concomitant with increasing anisotropy.

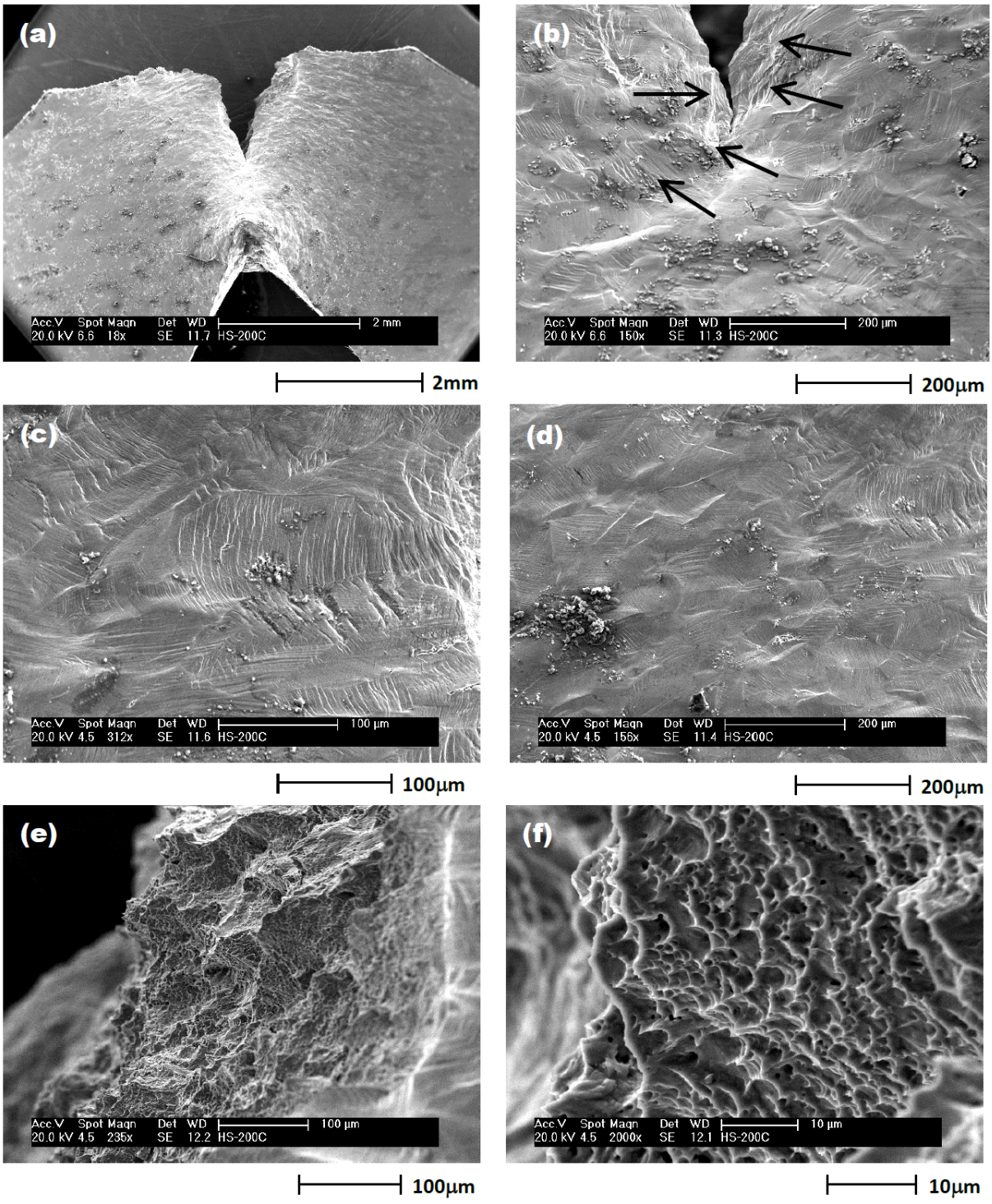

Fig. 2.4. SEM observations of the fractured specimen with concentration on crack edge in the specimen, the dislocation concentration along the crack, and fractured face with void formation at T=473 K. The arrows in (b) indicate the dense dislocation regions.

Remarkably, crack damage propagation does not even continue further to cause the full rupture of the specimen, i.e. less than ¼ of the material ligament remained connected even though it was highly distorted. Specifically, the upper half part of the specimen remains in predominantly compression state, suggesting that damage mechanisms on the fractured part are mostly facilitated by the tensile mode. Even if the shear fracture mode is present, it cannot be captured via SEM due to the very acute angle of the crack tip. Figs. 4e and f prove that the main mechanism of damage nucleation is void formation, such that the sub-micrometer size dimples – a feature of ductile fracture [36] – failed under tensile loading mode are evident. [2]

2.3.2. Constitutive relation and fracture criterion

Phenomenological constitutive relation proposed by Johnson and Cook [11] was chosen for the current study. The JC plasticity model computes the von Mises flow stress ($\bar{\sigma}$) behavior as a function of the equivalent plastic strain ($\bar{\varepsilon}^{pl}$) and equivalent plastic strain rate ($\dot{\bar{\varepsilon}}^{pl}$):

$$\bar{\sigma} = (A + B(\bar{\varepsilon}^{pl})^n)[1 + Cln(\dot{\bar{\varepsilon}}^{pl}/\dot{\bar{\varepsilon}}_0^{pl})](1 - T^{*m}) \quad (2.1)$$

In Eq. 2.1, A, B, C and m are constants; n is the strain hardening exponent; $\dot{\bar{\varepsilon}}^{pl}/\dot{\bar{\varepsilon}}_0^{pl}$ is the normalized equivalent plastic strain rate (typically normalized to a plastic strain of 1.0 s^{-1}); and T^* is the homologous temperature defined as:

$$T^* = (T - T_{room})/(T_{melt} - T_{room}) \quad (2.2)$$

In Eq. 2.2, T is the material temperature, T_{melt} is the melting temperature, and T_{room} is the room temperature. It has been demonstrated that the influence of temperature on the stress triaxiality is very limited [21]. Furthermore, the thermal softening effect observed in HS was

[2] The corresponding details are provided in *Section 4.2*.

not considered to be significant (see Fig. 2.3b), and therefore was neglected in the current study, while thermal softening related to the material temperature was accounted for.

In order to model failure of the material, Johnson-Cook failure criterion [11] was exploited, which is based on damage accumulation and has the basic form:

$$D = \sum \frac{\Delta \varepsilon_{eq}}{\varepsilon_f} \tag{2.3}$$

In Eq. 2.3, D is the damage to a material element, $\Delta \varepsilon_{eq}$ is the increment of accumulated plastic strain, and ε_f is the accumulated plastic strain to failure under the current conditions of the stress triaxiality, strain rate and temperature. The failure strain ε_f is defined as in Eq. 2.4, and failure occurs when D=1:

$$\varepsilon_f = (D_1 + D_2 \exp(D_3 \sigma^*))\left(1 + \dot{\bar{\varepsilon}}^*_{eq}\right)^{D_4}(1 + D_5 T^*) \tag{2.4}$$

where $D_1,\ldots, D_5$ are material constants, $\sigma^* = (\frac{\sigma_H}{\bar{\sigma}})_{av}$ is the stress triaxiality ratio and $\dot{\bar{\varepsilon}}^*_{eq} = \frac{\dot{\bar{\varepsilon}}^{pl}}{\dot{\bar{\varepsilon}}^{pl}_0}$ is the dimensionless strain rate.

2.3.3. Identification of material constants

In order to obtain constants of the JC material model we initially need material response data at quasi-static loading condition, yet over a wide range of strain rates. Empirically obtaining material and damage parameters with consideration of stress triaxiality and strain rate is challenging and costly. Hence, in order to avoid such experiments in the current work, it was preferred to exploit available data on high strain rate behavior of HS in literature in combination with some assumptions.

The term $(A + B(\bar{\varepsilon}^{pl})^n)$ in the JC material model is a Bodner-type hardening relationship, and to determine A, B and n, the experimentally obtained quasi-static true stress-strain response of the HS at a strain rate of 10^{-5} 1/s [6] was considered for simulations (Fig. 2.5).

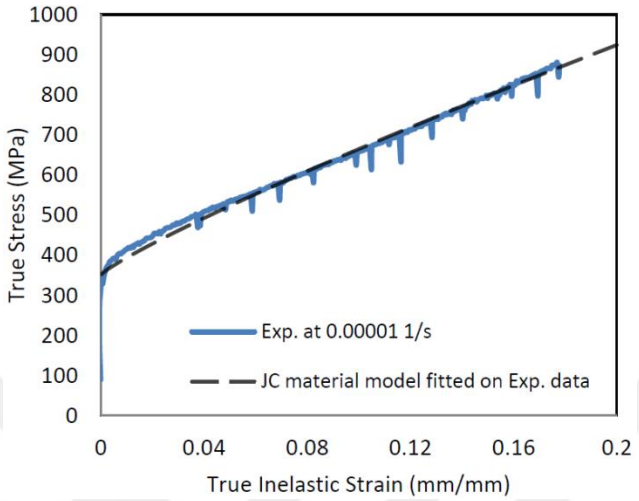

Fig. 2.5. Quasi-static true stress – inelastic strain curve of HS and fitted JC material model used in the FE analysis.

In order to obtain the term C in Eq. 2.1 and the terms D_4 and D_5 in the JC damage model, experimental high strain rate test data of a similar high-manganese steel reported in ref. [36] and ref. [2] was adopted (Fig. 2.6a and b). Here, it is assumed that the strain hardening and failure strain dependency on the strain rate would not be altered considerably due to slight dissimilarity in carbon content and adopted heat treatment [37]. The aforementioned parameters were calculated through a curve fitting procedure. D_1 was assumed to be the fracture strain of the plain material [2] under uniaxial tensile loading (specimen without a notch) in the given strain rate, and D_2 and D_3 were defined through a trial and error procedure, such that the damage curve passed uniaxial tensile failure strain of the HS horizontally within R1 and R2 regions and the vertical cut-off value for the fracture strain line constituted an asymptote of the damage curve (see Fig. 2.1). Performed sensitivity

analysis using different D_2 and D_3 showed independency of the FE result of these parameters, provided they stay at or lower than 0.01 and -15, respectively.

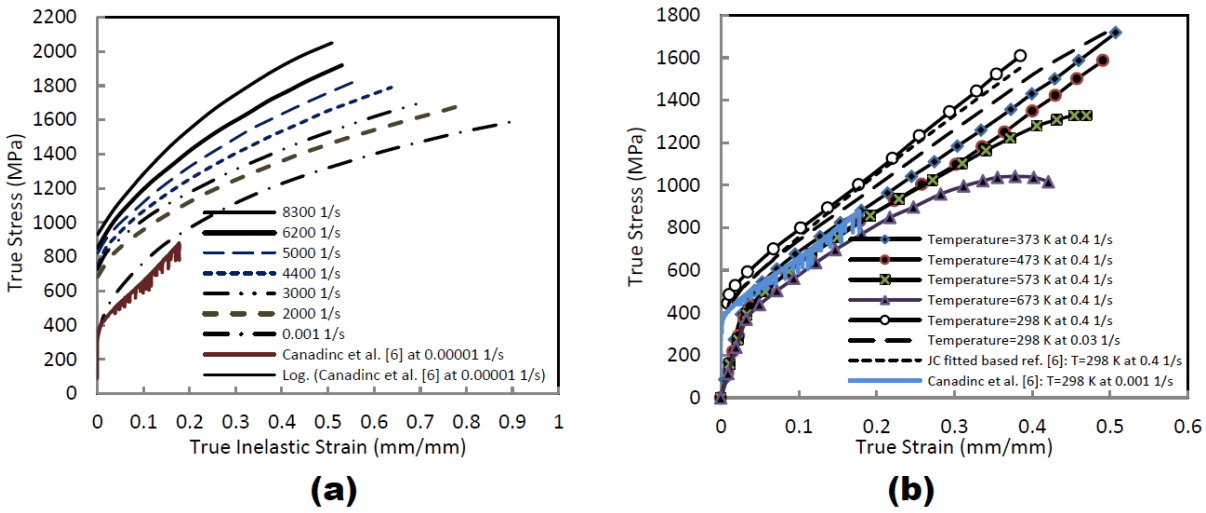

Fig. 2.6. **(a)** The room temperature strain rate dependence of the monotonic tensile deformation response of Hadfield steels used for calculation of parameter C: Each curve is representative of 3–5 experiments [36]; **(b)** High temperature dependence of the monotonic tensile deformation response of the HS [2] accompanied by the JC fitted curve for the room temperature and strain rate of 0.4 s^{-1}.

2.4. NUMERICAL MODELING AND DISCUSSION

2.4.1. Finite element simulations: macro-scale model

The explicit finite element ANSYS code with LS-DYNA solver [32] was employed to simulate the impact response of high-manganese HS in Charpy experiment. The eight-node solid elements with single point integration and stiffness-based hourglass (HG) control [38] were chosen for meshing the specimen and the hammer (see Fig. 2.7). Another set of surface-to-surface contact elements was employed at the outer surfaces of the specimen and the hammer, while two support beds were considered as rigid bodies. For all interfaces, the corresponding static and dynamic friction coefficients were set to 0.2 and 0.09, respectively [39].

Finite element results for problems involving strain localization and failure are highly sensitive to the element size [21]. Therefore, in the current work, the initial modeling was performed utilizing a coarse mesh, and then the distribution and size of the elements were modified within several steps to minimize discrepancy in deformation-time response. The best results were achieved using 30,690 brick elements for the impact specimen with a finer mesh in the notch region, where the element size was about 0.02 mm in dimension (Fig. 2.7).

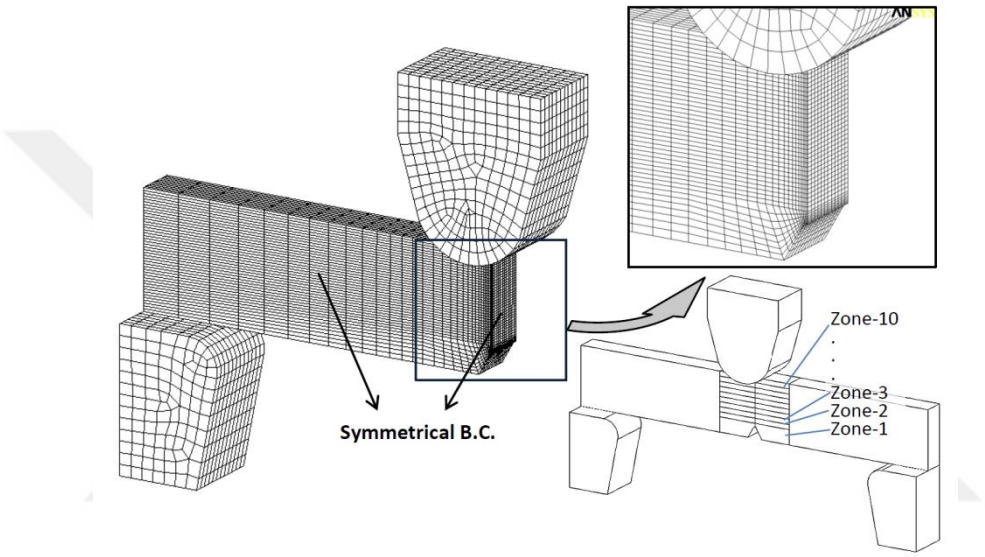

Fig. 2.7. Final FE mesh and impact specimen geometry discretization for calculation of the microstructural behavior for the next step of the numerical work: ten different zones were identified for crystal plasticity modeling.

The JC constitutive material constants employed in FE simulations are listed in Table 2.1 for HS, and for the hammer/striker a linear elastic material relationship was assumed with a Young's modulus of 200 GPa and a Poisson's ratio of 0.3. A nonlinear transient dynamic analysis was carried out to simulate the high strain rate loading of the impact specimen. To constrain the specimen and the hammer in the model, two fixed support beds were devised in accord with the original experimental setup (see Fig. 2.2). Only ¼ of the test set up with respect to the symmetrical Cartesian *X*-*Y* and *Y*-*Z* planes was simulated to reduce

computational time. The FE solution process was conducted within a single load step and with an initial maximum velocity of 3.80 m/s for the striker.

2.4.2. Finite element simulation results: macro-scale model

Based on the previously described conditions and projected JC material constants, the FE model was run primarily without consideration of the ductile fracture damage. Then, stress triaxiality factor (η) was analyzed in order to investigate suitability of the modified JC damage model assumptions for the calculation of D_1, D_2 and D_3. Despite the fact that η values are slightly higher inside the specimen (i.e. the middle of the thickness) than that of the surface, only the surface η values were analyzed here. It was also previously shown (section 2) that failure strains attributed to even higher η do not differ considerably from the η in uniaxial tensile tests during high strain rate loading.

Fig. 2.8 demonstrates η along the *Y*-direction of the specimen. It shows high stress triaxiality on the notch region fluctuates slightly for about 1/3 of the ligament before suddenly falling down to a negative value, and then it remained nearly constant (i.e. around or beyond the cut-off value for the fracture strain) for about ½ of the ligament. Furthermore, it is noted that, with the increase of the loading time steps, the η range decreased and moved towards the top of the specimen (i.e. where the striker impacted the specimen). Including the damage model in the initial FE model, when damage evolution (in the FE model achieved by element erosion) was taken into account, this graph was replicated over the remaining material ligament with the almost similar pattern (see Fig. 2.9). Fig. 2.9 clearly demonstrates that the η value for the cracked region remains around 0.45 during the fracture, which resembles the η of uniaxial tensile loading (specimen without a notch).

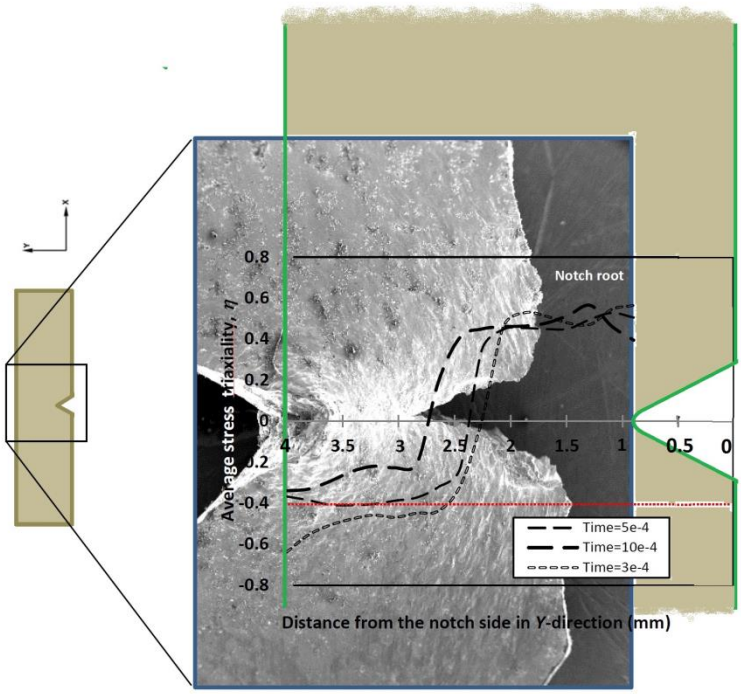

Fig. 2.8. Average stress triaxiality on the face-side of the smallest cross section on the *Y*-direction with horizontal representative of the cut-off value (explained in ref. [33]) of stress triaxiality.

Obviously, the sudden drop in the transient region in Fig. 2.8 – the drop in stress triaxiality on the distance between compression and tensile failure modes: R2 region in the (ε_f-η) graph (see Fig. 2.1) covers major part of the transient region – lies on the coincident neutral axis (NA) of the tearing impact specimen, which has theoretically near-to-zero strain amplitude (see Fig. 2.10). Hence, accumulated damage in this region is expected to be very small. Meanwhile, the notch root experiences high strain magnitudes and has a large accumulated damage value. As a result, the first element failures begin on the notch region through the tensile mode while elements located on the transient region never fail. In other words, the accumulated damage is not large enough in the transient region to cause failure of elements prior to failure of elements deforming in tensile mode (see Fig. 2.9). Thus, in the current simulation it was assumed that failure is governed merely by tensile and compressive modes. The SEM images of the fracture surfaces (Fig. 2.4) support this argument by evidencing that

the dominant damage mechanisms are the tensile and compressive modes rather than shear or combined modes: Fig. 2.4f shows void formation and their coalescence to the final tensile failure.

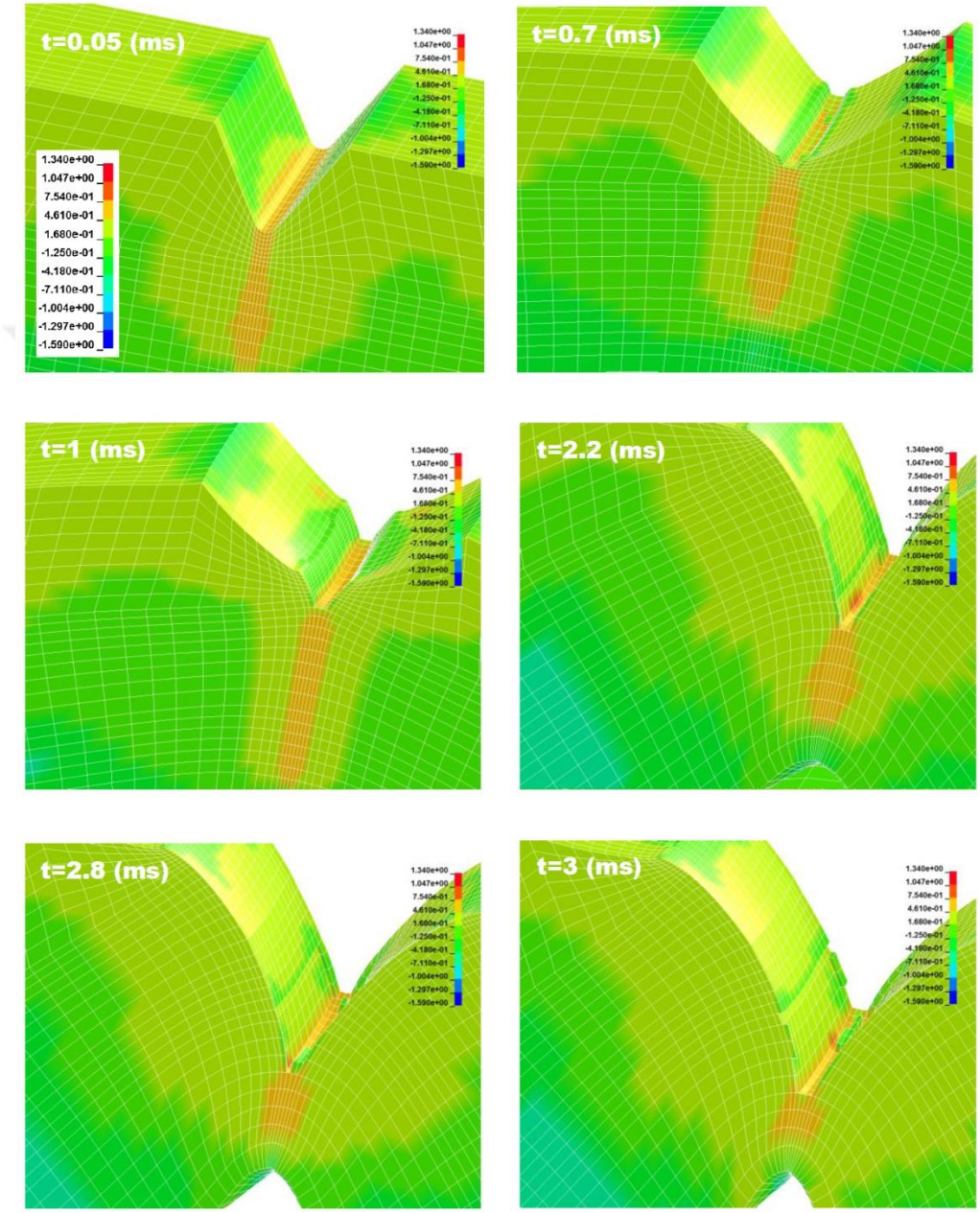

Fig. 2.9. Stress triaxiality parameter (η) distribution around the damage evolution region during ductile fracture.

The corresponding FE results show an incipient failure on the notch root within the middle of the thickness due to very large plastic strains (see Fig. 2.9: t=0.7 ms), and further damage development towards the outer edges of the notch root prior to growing inside the ligament of the specimen. Although failure strain in region R1 and region R2 should be captured based on test results, the triaxiality analysis provided herein proves that the only predominant fracture mechanism (along the hypothetical crack path) should be the tensile mode in the specific case of Charpy impact test (see Fig. 2.9). For this reason, it was assumed that failure strain remains constant at the failure strain of tensile specimen due to void formation under the applied strain rate. The JC damage parameters utilized in this study are tabulated in Table 2.1.

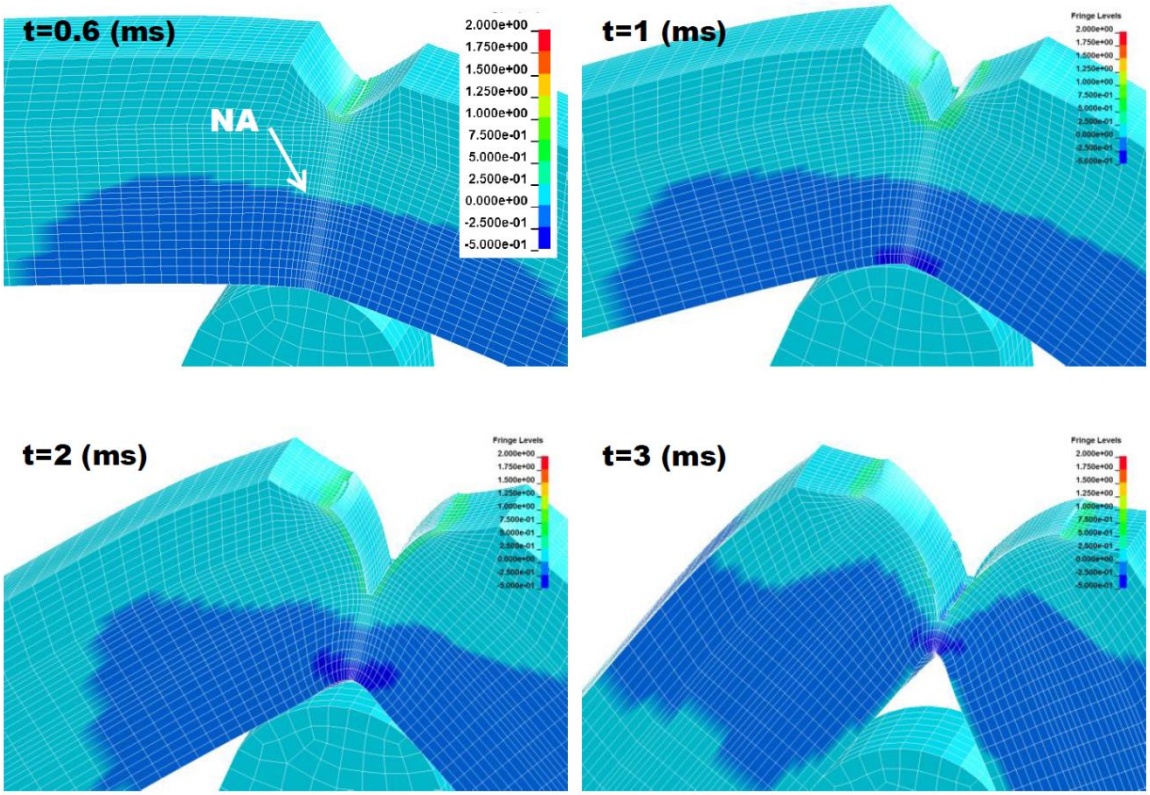

Fig. 2.10. Strain (mm/mm) distribution along *X*-direction emphasizing the position of the *neutral axis* (NA) over four different steps of the deformation sequences during impact. Contour levels for strain are restricted between -0.5 and 2 in order to represent the location of NA more clearly.

Table 2.1. Material constants for the HS and JC constitutive material relation and the JC damage criterion.

Elastic constants and density			Yield stress and Strain hardening			Strain rate hardening	
E (GPa)	ν	ρ (Kg/m^3)	A (MPa)	B (MPa)	n	$\dot{\varepsilon}_0^{pl}$	C
210	0.33	7750	361	2625	0.87	1×10^{-3}	0.023

JC fracture strain constants					Temperature softening			
D_1	D_2	D_3	D_4	D_5	C_p (J/Kg.K)	T_m (K)	T_0 (K)	m
0.925	0.01>	-15.00>	-0.018	1.12	490	1653	323	0.94

Once all the JC damage model constants were determined, the FE simulation was repeated by incorporating the calculated ductile fracture damage parameters reported in Table 2.1. In the FE simulations the original stiffness of the failed elements were multiplied by a very small number, reducing element stiffness, and demonstrating the element erosion, and thereby modeling the ductile damage progression. As shown in Fig. 2.11, the predicted force-time response of the HS yielded an overestimation of the force and impact energy using a coarse mesh, while the final fracture of the specimen was predicted agreeably well. Interestingly, utility of a finer mesh underestimates the impact energy while the peak force remains almost unaltered (Fig. 2.11).

Fig. 2.11 asserts that application of the macroscopic plasticity is unable to predict impact response of HS that has a very complicated strain hardening mechanism [40], and significantly overestimates the impact force. This clearly demonstrates the need for a versatile method capable of accurately predicting impact response of HS or similar polycrystalline alloys with complicated micro-deformation activities.

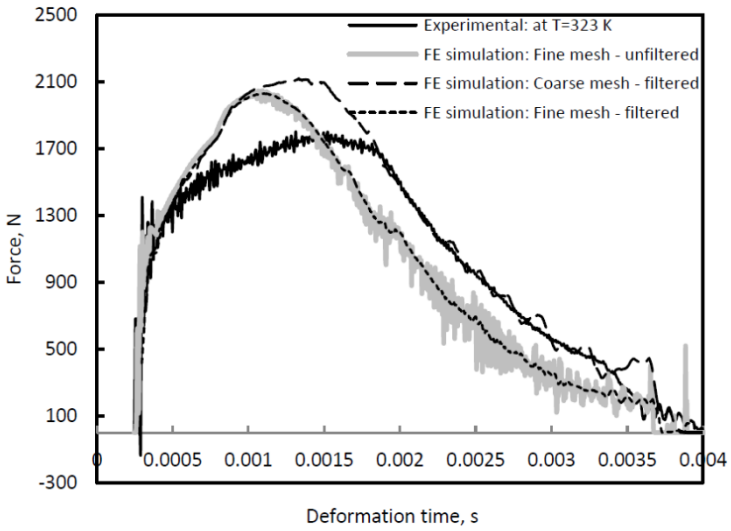

Fig. 2.11. Initial simulation of the impact force vs. time response of HS with the application of JC material and damage model – JC material and fracture constants are cited in Table 2.1.

2.4.3. Micro-scale model

Primary FE simulation of the impact divulges insufficiency of the application of uniaxial quasi-static material data to capture the experimental force-deformation behavior of HS. In fact, the influence of highly heterogonous microstructural features and micro-deformation mechanisms are shadowed in the initial macro-scale FE modeling effort. Thus, exploiting a flow rule based on micro-deformation mechanisms that can properly reflect the geometry and loading boundary condition effects has become evident. In the current multi-scale modeling approach, the VPSC crystal plasticity algorithm was implemented into the FE model, such that the roles of texture and the corresponding plastic anisotropy could be accounted for. While another way of establishing such a flow rule could be running multi-axial experiments, an alternative can be based on crystal plasticity modeling. In particular, a crystal plasticity model not only predicts the macroscopic deformation of a material, but more importantly, it also captures the deformation characteristics at the slip system level [41]. Once correctly formulated and verified with experimental data, such a model should predict the deformation

response for any type of loading scenario [42]. This gives way to an alternative approach, such that the deformation of high-manganese HS can be modeled at the microscopic level based on the experimentally obtained uniaxial deformation response specific to individual regions with varying degrees of plastic anisotropy. The current modeling approach achieved this by calculation of the velocity gradient in individual zones and updating the corresponding boundary condition of each zone in the VPSC model, resulting in an updated material flow behavior.

The inverse pole figure provided in Fig. 2.12b demonstrates the initial texture and the corresponding anisotropy of the microstructure of the Hadfield steel tested in this work. Specifically, the initial texture was measured by XRD to obtain Euler angles and their weights within a data file that was provided as an input to the VPSC. The experimentally measured initial texture of the material (Fig. 2.12b) and the experimentally obtained deformation response under uniaxial quasi-static tensile loading (see Fig. 2.12a) were utilized in order to calibrate microstructural response in VPSC crystal plasticity model based on Voce hardening flow law [43].

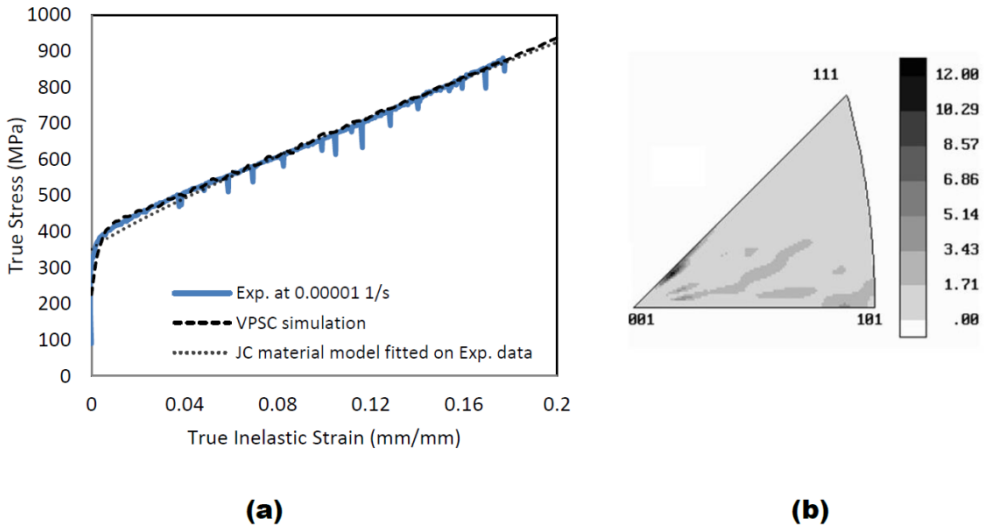

Fig. 2.12. (a) Quasi-static true-stress inelastic strain curve of HS used in the VPSC crystal plasticity simulation and initial VPSC modeling results: One should note that these experiments were aborted at

about 18% of strain. (b) Inverse pole figure demonstrating the texture and anisotropy of HS along the loading direction of the sample (the data was obtained from XRD measurements).

The VPSC algorithm employed in the current study considers the plastic deformation when one or more slip or twinning systems become active. For a system (s), the corresponding resolved shear stress (τ^s_{RSS}) driving plastic deformation is defined in terms of the vector forms of the Schmid tensor (m^s_i) and the applied stress (σ_i) as:

$$\tau^s_{RSS} = m^s_i \sigma_i \tag{2.5}$$

The nonlinear shear strain rate in the system s can be described as a function of τ^s_{RSS}:

$$\dot{\gamma}^s = \dot{\gamma}_0 \left(\frac{\tau^s_{RSS}}{\tau^s_0} \right)^n = \dot{\gamma}_0 \left(\frac{m^s_i \sigma_i}{\tau^s_0} \right)^n \tag{2.6}$$

where $\dot{\gamma}_0$ is a reference rate, τ^s_0 is the threshold stress corresponding to this reference rate, and n is the inverse of the rate sensitivity index. The superposition of the contributions from all active systems gives the total strain rate in a crystal, which can be presented in its pseudolinearized form as in the following expression [40]:

$$\dot{\varepsilon}_i = \left[\dot{\gamma}_0 \sum_1^s \frac{m^s_i m^s_j}{\tau^s_0} \left(\frac{m^s_k \sigma_k}{\tau^s_0} \right)^{n-1} \right] \sigma_j = M^{c(\mathrm{sec})}_{ij} \left(\tilde{\sigma} \right) \sigma_j \tag{2.7}$$

where $M^{c(\mathrm{sec})}_{ij}$ is the secant visco-plastic compliance of the crystal which gives the instantaneous relation between stress and strain rate. At the polycrystal level, this relationship assumes the following form:

$$\dot{E}_i = M^{(\mathrm{sec})}_{ij} \left(\tilde{\Sigma} \right) \Sigma_j + \dot{\Sigma}^0 \tag{2.8}$$

where $\dot{E}_i$ and Σ represent the polycrystal strain rate and applied stress, respectively.

In a continuum that consists of a matrix and inclusions, the deviations in strain rate and stress between the inclusion and their overall magnitudes are defined as

$$\dot{\tilde{\varepsilon}}_k = \dot{\varepsilon}_k - \dot{E}_k \tag{2.9}$$

$$\tilde{\sigma}_j = \sigma_j - \Sigma_j \tag{2.10}$$

where $\dot{\varepsilon}_k$ and σ_j stand for the local (single crystal or grain level) strain rate and stress. Utilizing Eshelby's inhomogeneous inclusion formulation one can solve the stress equilibrium equation to derive [43]:

$$\dot{\tilde{\varepsilon}} = -\tilde{M} : \tilde{\sigma} \tag{2.11}$$

The interaction tensor $\tilde{M}$ is defined as

$$\tilde{M} = n'(I - S)^{-1} : S : M^{(\sec)} \tag{2.12}$$

where $M^{(\sec)}$ is the secant compliance tensor for the polycrystal aggregate and S is the visco-plastic Eshelby tensor [43].

Substitution of Eqs. 2.7 and 2.8 into Eq. 2.11 yields the macroscopic secant compliance, $M^{(\sec)}$, and the macroscopic strain rate is evaluated by taking the weighted average of crystal strain rates over all the grains as in Eq. 2.13:

$$M^{(\sec)} = \left\langle M^{c(\sec)} : \left(M^{c(\sec)} + \tilde{M}\right)^{-1} : \left(M^{(\sec)} + \tilde{M}\right) \right\rangle \tag{2.13}$$

Iterative solution of the Eqs. 2.7, 2.11 and 2.13 gives the stress in each grain, the crystal's compliance tensor, and the polycrystal compliance consistent with the applied strain rate $\dot{E}_i$.

In this work, the term n in Eq. 2.6 was chosen as 20, which makes the formulation rate insensitive. As for the interaction Eq. 2.12, an effective value of n'=1 was used, which ensures a rigid interaction [40].

The rate of overall dislocation density can be expressed as:

$$\dot{\rho} = \sum_{n} \left\{ k_1 \sqrt{\rho} - k_2 \rho \right\} \left| \dot{\gamma}^n \right| \tag{2.14}$$

where k_1 and k_2 are geometric constants that define the athermal (statistical) storage of the moving dislocations [43]. The flow stress τ is defined in the traditional Taylor hardening format as:

$$\tau - \tau_0 = \alpha \mu b \sqrt{\rho} \tag{2.15}$$

where α is the dislocation interaction parameter and τ_0 is a reference strength, which is related to deformation at the grain level. From Eq. 2.15, with τ_0 constant, the rate of the flow stress is obtained by taking the time derivative as,

$$\dot{\tau} = \frac{\alpha \mu b \dot{\rho}}{2\sqrt{\rho}} \tag{2.16}$$

Substituting Eq. 2.14 into Eq. 2.16 results in:

$$\dot{\tau} = \sum_{n} \left\{ k_1 \frac{\alpha \mu b}{2} - k_2 \frac{\alpha \mu b}{2} \sqrt{\rho} \right\} \left| \dot{\gamma}^n \right| \tag{2.17}$$

From Eq. 2.15, the following identity is obtained for the square root of the density of dislocations:

$$\sqrt{\rho} = \frac{\tau - \tau_0}{\alpha \mu b} \tag{2.18}$$

Once Eq. 2.18 is substituted into Eq. 2.17, the rate of flow stress evolution is given by:

$$\dot{\tau} = \sum_n \left\{ k_1 \frac{\alpha \mu b}{2} - k_2 \frac{(\tau - \tau_0)}{2} \right\} \left| \dot{\gamma}^n \right| \tag{2.19}$$

One should note that the term $\left\{ \frac{\alpha \mu b}{2} k_1 - \frac{(\tau - \tau_0)}{2} k_2 \right\}$ in Eq. 2.19 is the linear Voce hardening term (Eq. 2.21). Having noted this, Eq. 2.19 can also be expressed as [43]:

$$\dot{\tau} = \sum_n \left\{ \theta_0 \left(\frac{\tau_s - \tau}{\tau_s - \tau_0} \right) \right\} \left| \dot{\gamma}^n \right| \tag{2.20}$$

where θ_0 is the constant strain hardening rate, and τ_s represents the saturation stress in the absence of geometric effects, or the threshold stress. The hardening is defined by an extended Voce law [43], which is characterized by the evolution of the threshold stress (τ^s) with accumulated shear strain (Γ) in each grain of the form

$$\tau^s = \tau_0 + (\tau_1 + \theta_1 \Gamma) \left(1 - \exp\left(- \frac{\theta_0 \Gamma}{\tau_1} \right) \right) \tag{2.21}$$

where τ_0 is the reference strength, and τ_1, θ_0 and θ_1 are the parameters that define the hardening behavior [43]. The hardening law defined by Eq. 2.21 characterizes the onset of plasticity and the saturation of threshold stress at larger strains.

The Voce hardening parameters that define the work hardening response of HS at the microscopic scale are tabulated in Table 2.2. The corresponding VPSC simulation results agree well with the experimental data (Fig. 2.12a). An exception is the onset of initial plastic deformation, where dislocation - grain boundary interactions and grain boundary misorientation angle distribution significantly dictate the stress level. These effects were not considered in the current work as a detailed treatment is needed for their proper incorporation

into VPSC, which was previously accomplished by the authors [41] and stays beyond the scope of the current study. One should note that the effects of strain rate and temperature were not included in this VPSC crystal plasticity model.

2.4.4. Multi-scale modeling approach

Even though uniaxial tensile test results have been utilized universally in numerical simulations of material response, it was shown that such data does not necessarily result in correct simulation of the material response because they cannot include the effect of micro-size features and micro-deformation mechanisms in the macro-scale deformation [39]. On the other hand, it was earlier documented that macroscopic response of HS is highly influenced by its complicated microstructural features [35, 40]. Therefore, proper consideration of the micro-deformation mechanisms is a prerequisite for accurate prediction of highly anisotropic polycrystalline metals such as HS. In order to take into account the plastic anisotropy due to the micro/grain size deformation mechanisms, the primary FE model was hired in order to establish the boundary conditions of a material point, including geometrical stress multi-axiality through deformation gradient matrix. Simultaneously, the VPSC plasticity model was calibrated incorporating the Voce hardening constitutive model based on the experimental quasi-static uniaxial tensile deformation response (see Fig. 2.12). Then, the computed velocity gradient in the initial FE model was introduced into the calibrated VPSC algorithm as a modified boundary condition, which introduces a new loading (a realistic multi-axial loading) scheme for a material point. Thus, in the updated VPSC model, the material hardening and flow rule were re-calculated in accord with the updated loading condition such that the effects of microstructural features and deformation mechanisms could be included. In the final step, employing an updated FE model, the original material data were replaced by

the computed microstructurally-informed material model through the re-calibration of the JC constitutive and damage model – that is, JC material model constants were re-calculated based on the updated microstructural-sensitive material flow behavior besides the original *C* and *m*.

In this paper, we demonstrate the appropriateness of this multi-scale methodology utilizing a relatively coarse 2D through-the-thickness discretization model for the updated material behavior. The designated 2D model is based on the initial numerical analysis which revealed that the velocity gradient remained nearly the same through the thickness of the specimen. Moreover, the effect of the damage propagation on the velocity gradient is not taken into account for simplicity. Ten equally-spaced domains (0.3 mm in *Y*-direction) along the middle section of the specimen were vertically distinguished for the loading boundary condition update (see Fig. 2.7). Average velocity gradient of the each segment at the middle section of the specimen was derived and introduced as a new boundary condition to the microstructural simulation. The schematic provided in Fig. 2.13 summarizes the numerical modeling approach adopted in this study.

To compute the velocity gradient in the FE model, a simplified approach was adopted based on the geometry and boundary conditions specific to the current Charpy impact experiments. Since the most important site for damage initiation and propagation is the notch region along the anticipated crack path, this region was the main focus of the current modeling approach.

Defining F_{ij} as deformation gradient tensor, and L_{ij} as velocity gradient tensor, it can be shown that $L_{ij} = \dot{F}_{ik}F_{kj}^{-1}$. Noting that $F_{ij} = R_{ik}U_{kj}$ and $R_{ij}^{-1} = R_{ji}$, velocity gradient can be derived as:

$$L_{ij} = R_{ik}(\dot{U}_{kl}U_{lm}^{-1})\,R_{jm} + \dot{R}_{ik}R_{jk} \tag{22}$$

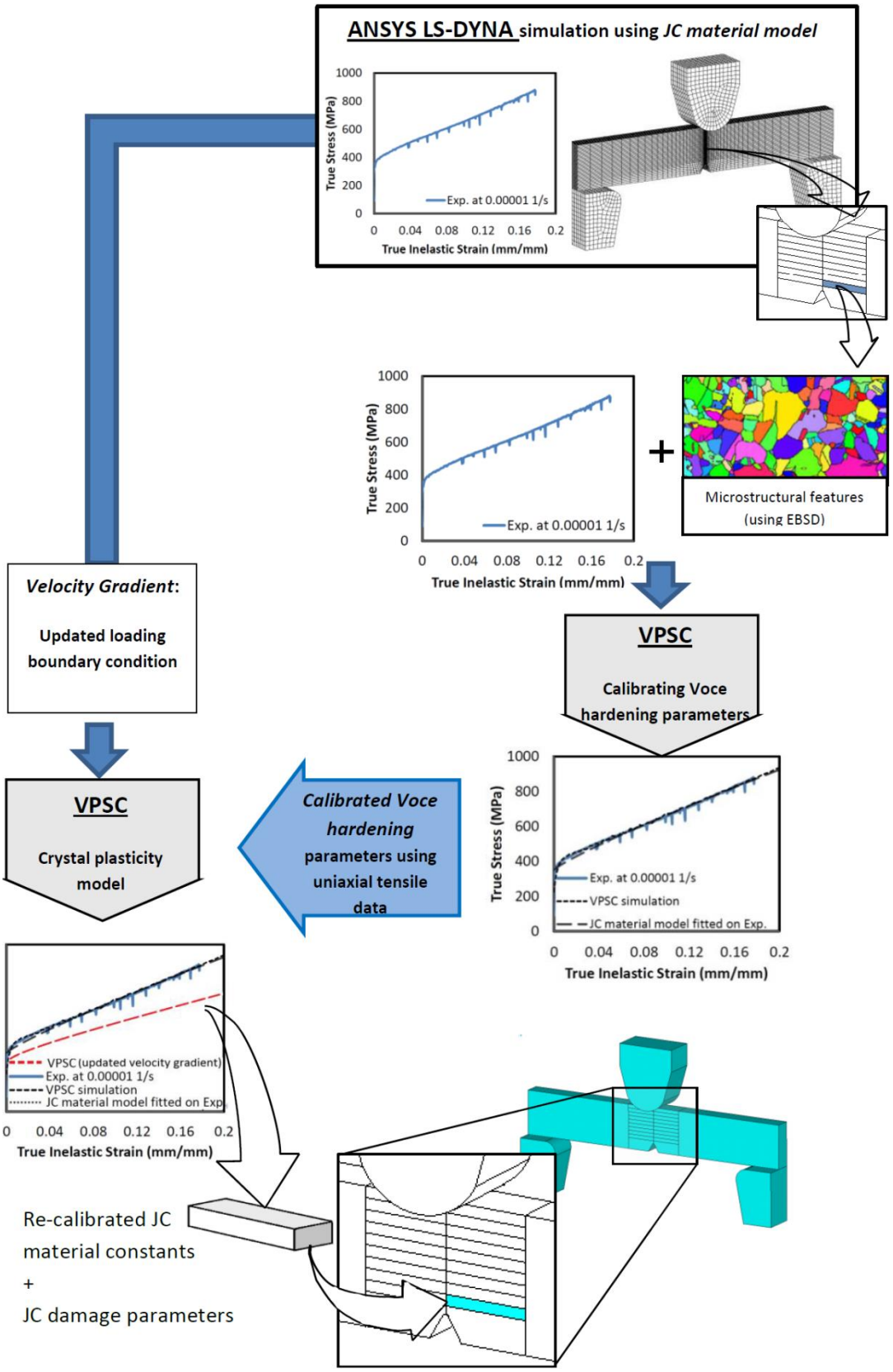

Fig. 2.13. Schematic illustration of the employed approach in numerical simulation of the impact response of high manganese steel.

In fact, the major part of the deformation is restricted to the middle cross section of the impact specimen, which governs the mechanics of impact during high loading regimes (Fig. 2.4a). Whilst the elements located on the *Y-Z* symmetry plane experience a very large tensile stretch, rotation in these elements is significantly small, and the assumption of *no rigid body rotation* will not be out of hand. Given this simplification, R_{ij} would be the *Identity* matrix, so $F_{ij} = U_{ij}$ and the Eq. 2.22 will be reduced to:

$$L_{ij} = \left(\dot{U}_{ik}\, U_{kj}^{-1}\right) \tag{2.23}$$

Taking the classical *infinitesimal strain* tensor as:

$$\epsilon_{ij} = \frac{1}{2}\left(F_{ij} + F_{ji}\right) - \delta_{ij} \tag{2.24}$$

and using the properties of U_{ij} which is symmetric, $U_{ji} = U_{ij}$ and $R_{ij} = \delta_{ij}$ then the Eq. 2.24 can be substituted by $\epsilon_{ij} = U_{ij} - \delta_{ij}$. Therefore, U_{ij} matrix was computed using strain matrix obtained through the initial FE simulation. L_{ij} was calculated for desired material point using Eq. 2.23 and numerical calculation of $\dot{U}_{ij} = \dot{F}_{ij}$ employing $\dot{U}_{ij} = \frac{1}{\Delta t}(U_{ij}^{t+\Delta t} - U_{ij}^{t})$ approximation and Δt = 0.0001 ms. Later, the obtained velocity gradient at desired material point was normalized according to the simple tensile loading velocity gradient (see Table 2.2 for the list of velocity gradient components for each of the ten zones computed in the current simulation). New boundary conditions were introduced to VPSC in form of *updated* normalized velocity gradients for the material. To do so, a new material response was computed based on the microstructural deformation mechanics subjected to an updated loading boundary condition. Eventually the estimated material responses in the notch region were averaged and incorporated into the final FE simulation though recalibration of the JC constitutive model as a unique material property for the whole specimen: Computed JC

constitutive model parameters in the final multiscale approach are A = 300, B = 2325 and n = 0.92.

Table 2.2. Microstructural material parameters and employed velocity gradient in the current multiscale modeling effort.

Voce hardening constitutive model constants				Strain rate hardening	
τ_1 (MPa)	τ_0 (MPa)	θ_1	θ_0	$\dot{\varepsilon}_0^{pl}$	n
135	132	480	8×10^3	1×10^{-5}	20

	Normalized velocity gradient components								
	L_{11}	L_{22}	L_{33}	L_{12}	L_{13}	L_{21}	L_{23}	L_{31}	L_{32}
Uniaxial tensile	1	-0.50	-0.50	0	0	0	0	0	0
Zone-1	1	2.58	-3.58	-0.4	0	0.026	0	0	0
Zone-2	1	1.29	-2.29	0.82	-0.69	-1.15	-2.91	0.64	1.11
Zone-3	1	-0.51	-0.49	-0.04	0.07	0.07	-0.14	0.04	-0.13
Zone-4	1	-0.33	-0.67	0	0	0.28	0.37	0	0.36
Zone-5	1	0	-1	0	0	0	0.33	0	0.34
Zone-6	1	-0.16	-0.84	0	0	0	0	0	0
Zone-7	1	-0.26	-0.74	0	0.17	0	0	0.16	0
Zone-8	1	-0.34	-0.66	0	0	0	0	0	0
Zone-9	1	-0.51	-0.49	-0.06	0	-0.07	0.23	0	0.23
Zone-10	1	-0.57	-0.43	-0.012	0	-0.06	-0.07	0	-0.07

Improved FE simulation results upon incorporating the VPSC model are evident in Fig. 2.14: the proposed multi-scale approach successfully predicts the impact response of HS throughout the whole deformation. The corresponding deformation spectrum of the specimen over impact time is demonstrated in Fig. 2.15. For a better assessment of the simulation results, results of a fully modeled specimen (not the symmetric quarter) are provided here as an example. In particular, the von-Mises stress distribution clearly demonstrates the concentration of the stresses along the notch region beneath the notch edge and the hammer

side. It is also noted that the deformation of the cross section of the impact specimen agrees well with the experimental observations (see Fig. 2.16). Specifically, the simulation results shown in Fig. 2.16 confirm that the impact specimen is not totally separated following fracture failure and two parts are still attached to each other. Even though the predicted ligament in the failed specimen is a little smaller than that observed following the experiments, the shapes of the fractured surfaces strikingly resemble the failed cross section of the specimen (Fig. 2.16).

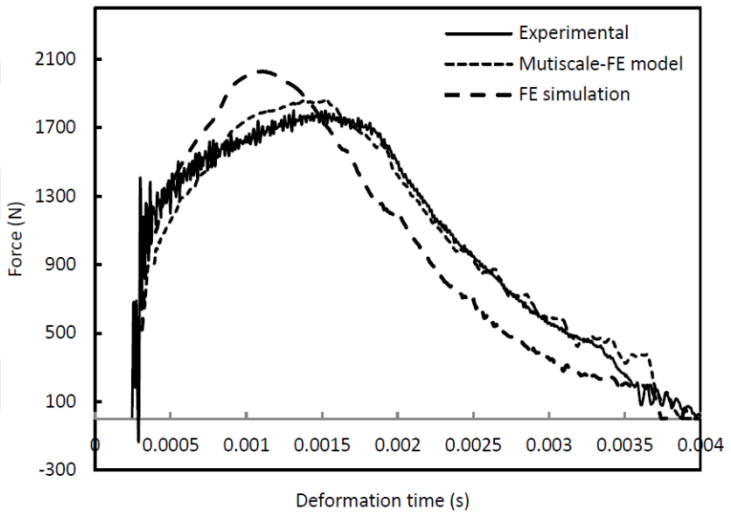

Fig. 2.14. Multiscale FE prediction of the impact force vs. time response of HS with the application of JC material and damage model: Comparison between FE and proposed multiscale FE model.

An important remark has to be made at this point regarding the simulation results. While all the simplifying assumptions in the computational analysis contribute to a discrepancy between simulation and experimental results, extracting some of the macroscopic material data using the data in literature (and microscopic material data using the same material tested by authors) may have affected the predicted response to a certain extent.

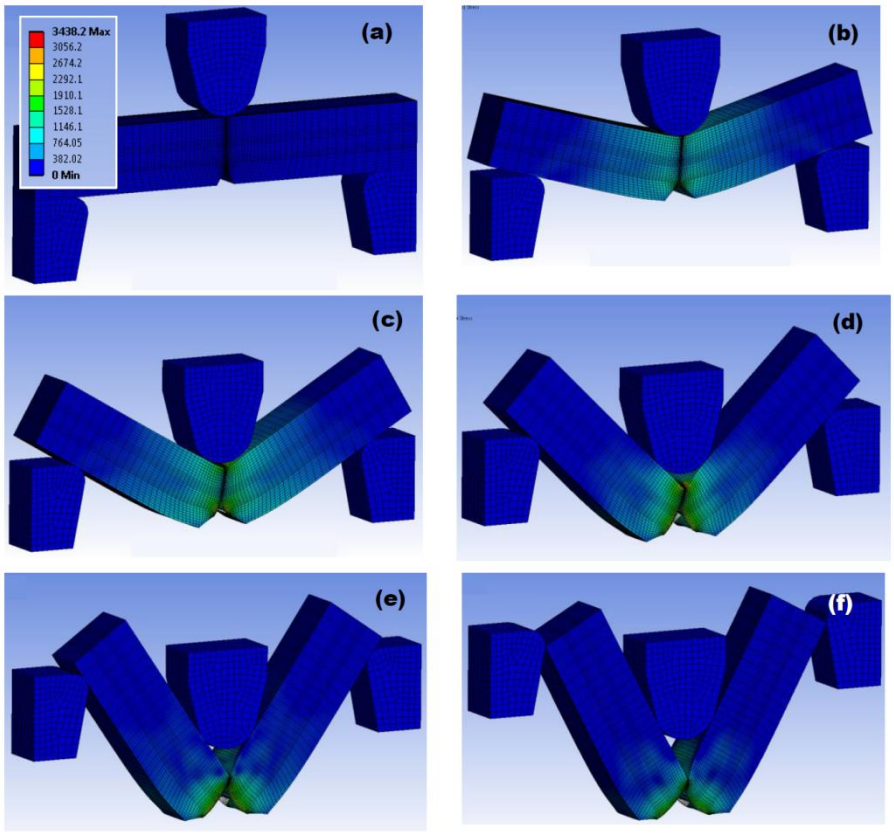

Fig. 2.15. Von-Mises stress (MPa) distribution and deformation sequences during ductile fracture of the whole sample.

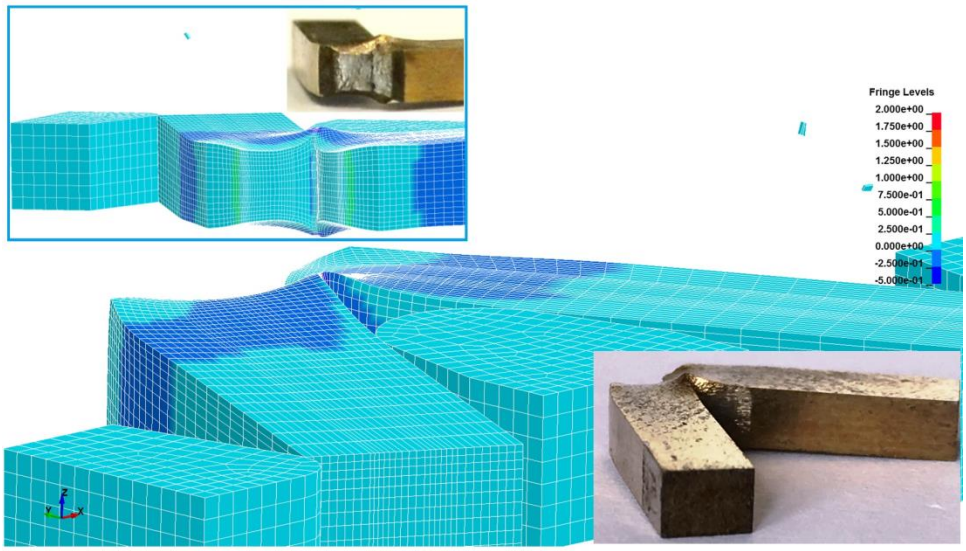

Fig. 2.16. Strain (mm/mm) distribution along *X*-direction at the end of the deformation illustrating protruded regions behind the striker (under high compressive loads) and mirrored picture of the cracked surfaces after fracture (under the notch) on the top. Photos show the actual samples following the experiments.

2.5. Concluding remarks

The multi-scale modeling approach presented in this paper was proposed with the aim of incorporating the effects of microstructure and plastic anisotropy into large-scale finite element (FE) modeling of impact response of polycrystalline metals. As a case study, an high-manganese austenitic steel, namely the Hadfield steel (HS), was studied where the application of conventional plasticity models fall short of precisely predicting the impact deformation behavior. For this purpose, following the initial explicit FE simulations employing quasi-static uniaxial data, inelastic strain history of the impact specimen was analyzed in order to obtain velocity gradient of the material. The calculated velocity gradient of each zone constituted an updated boundary condition for the primarily calibrated microstructural crystal plasticity model. As a result, the influence of microstructural features and potential micro-deformation mechanisms were introduced in the macro-scale FE model as a new material property through recalibration of the JC material parameters. Simulation results confirm the capability of the proposed modeling approach in predicting the microstructure-sensitive macroscopic response of HS. Significant improvement of the impact response estimation using this multi-scale model over the conventional FE models is a solid proof of the asserted claim. We draw the following conclusions based on the work presented herein:

- FE simulation predicts highly compressive and tensile stress triaxiality fields in the notch region. However, transient/shear triaxiality in the specimen allocated a tiny space to itself, and even stress triaxiality of this small district is swapped by the tensile triaxiality mode following the crack growth during the dynamic loading. Since the elements located on the transient region do not fail prior to the failure of the elements in tensile region, the

majority of the ligament eventually fails in the tensile mode. This confirms the utility of the JC damage model for prediction of the Charpy impact test results.

- Consideration of the geometry-dependent multi-axiality in loading state plays significant role on the hardening response of polycrystalline metals with highly anisotropic microstructures. Consequently, using uniaxial tensile testing data as constitutive relationship in impact simulations should not be expected to yield precise estimation of force and impact energy.
- Results obtained through the application of the proposed microstructurally-informed multi-scale model that incorporates the visco-plastic self-consistent (VPSC) crystal plasticity model into the Johnson-Cook (JC) material and damage model stand in a very good agreement with the experimental observations in terms of force, energy and macroscopic distortion of body features.

Finally, this study can be exploited by the industry, where a need for a decoupled formulation for microstructurally-informed prediction of the macroscopic response of the material under high velocity loading is pursued.

BIBLIOGRAPHY

1. Armstrong, R. W., & Walley, S. M. (2008). High strain rate properties of metals and alloys. *International Materials Reviews*, *53*(3), 105-128.
2. Bayraktar, E., Khalid, F. A., & Levaillant, C. (2004). Deformation and fracture behaviour of high manganese austenitic steel. *Journal of Materials Processing Technology*, *147*(2), 145-154.
3. Adler, P. H., Olson, G. B., & Owen, W. S. (1986). Strain hardening of Hadfield manganese steel. *Metallurgical and Materials Transactions A*, 17(10), 1725-1737.
4. Li, Y., Zhu, L., Liu, Y., Wei, Y., Wu, Y., Tang, D., & Mi, Z. (2013). On the strain hardening and texture evolution in high manganese steels: experiments and numerical investigation. *Journal of the Mechanics and Physics of Solids*, *61*(12), 2588-2604.
5. Canadinc, D., Sehitoglu, H., Maier, H. J., Niklasch, D., & Chumlyakov, Y. I. (2007). Orientation evolution in Hadfield steel single crystals under combined slip and twinning. *International journal of solids and structures*, *44*(1), 34-50.
6. Canadinc, D., Efstathiou, C., & Sehitoglu, H. (2008). On the negative strain rate sensitivity of Hadfield steel. *Scripta Materialia*, *59*(10), 1103-1106.
7. Tucker, M. T., Horstemeyer, M. F., Gullett, P. M., El Kadiri, H., & Whittington, W. R. (2009). Anisotropic effects on the strain rate dependence of a wrought magnesium alloy. *Scripta Materialia*, 60(3), 182-185.
8. Bal, B., Gumus, B., Gerstein, G., Canadinc, D., & Maier, H. J. (2015). On the micro-deformation mechanisms active in high-manganese austenitic steels under impact loading. *Materials Science and Engineering: A*, 632, 29-34.
9. Cockcroft, M. G., & Latham, D. J. (1968). Ductility and the workability of metals. *J Inst Metals*, *96*(1), 33-39.
10. Gurson, A. L. (1977). Continuum theory of ductile rupture by void nucleation and growth: Part I—Yield criteria and flow rules for porous ductile media. *Journal of engineering materials and technology*, *99*(1), 2-15.
11. Johnson, G. R., & Cook, W. H. (1983, April). A constitutive model and data for metals subjected to large strains, high strain rates and high temperatures. In *Proceedings of the 7th International Symposium on Ballistics* (Vol. 21, pp. 541-547).
12. Zerilli, F. J., & Armstrong, R. W. (1987). Dislocation-mechanics-based constitutive relations for material dynamics calculations. *Journal of Applied Physics*, *61*(5), 1816-1825.
13. Børvik, T., Hopperstad, O. S., Berstad, T., & Langseth, M. (2001). A computational model of viscoplasticity and ductile damage for impact and penetration. *European Journal of Mechanics-A/Solids*, *20*(5), 685-712.

14. Dey, S., Børvik, T., Hopperstad, O. S., & Langseth, M. (2007). On the influence of constitutive relation in projectile impact of steel plates. *International Journal of Impact Engineering*, *34*(3), 464-486.

15. Xue, L., & Wierzbicki, T. (2008). Ductile fracture initiation and propagation modeling using damage plasticity theory. *Engineering Fracture Mechanics*,*75*(11), 3276-3293.

16. El-Magd, E., & Abouridouane, M. (2006). Characterization, modelling and simulation of deformation and fracture behaviour of the light-weight wrought alloys under high strain rate loading. *International journal of impact engineering*, *32*(5), 741-758.

17. Brünig, M., & Gerke, S. (2011). Simulation of damage evolution in ductile metals undergoing dynamic loading conditions. *International Journal of Plasticity*, *27*(10), 1598-1617.

18. Nahshon, K., & Hutchinson, J. W. (2008). Modification of the Gurson model for shear failure. *European Journal of Mechanics-A/Solids*, *27*(1), 1-17.

19. Nahshon, K., & Xue, Z. (2009). A modified Gurson model and its application to punch-out experiments. *Engineering Fracture Mechanics*, *76*(8), 997-1009.

20. Wang, X., & Shi, J. (2013). Validation of Johnson-Cook plasticity and damage model using impact experiment. *International Journal of Impact Engineering*, *60*, 67-75.

21. Børvik, T., Hopperstad, O. S., & Berstad, T. (2003). On the influence of stress triaxiality and strain rate on the behaviour of a structural steel. Part II. Numerical study. *European Journal of Mechanics-A/Solids*, *22*(1), 15-32.

22. Børvik, T., Hopperstad, O. S., Pedersen, K. O. (2010). Quasi-brittle fracture during structural impact of AA7075-T651 aluminium plates. *International Journal of Impact Engineering*, *37*, 537–551.

23. Hopperstad, O. S., Børvik, T., Langseth, M., Labibes, K., & Albertini, C. (2003). On the influence of stress triaxiality and strain rate on the behaviour of a structural steel. Part I. Experiments. *European Journal of Mechanics-A/Solids*, *22*(1), 1-13.

24. Bao, Y., & Wierzbicki, T. (2004). On fracture locus in the equivalent strain and stress triaxiality space. *International Journal of Mechanical Sciences*, *46*(1), 81-98.

25. Bao, Y., & Wierzbicki, T. (2004). A comparative study on various ductile crack formation criteria. *Journal of Engineering Materials and Technology*, *126*(3), 314-324.

26. Tanguy, B., Besson, J., Piques, R., & Pineau, A. (2005). Ductile to brittle transition of an A508 steel characterized by Charpy impact test: Part II: modeling of the Charpy transition curve. *Engineering fracture mechanics*, *72*(3), 413-434.

27. Eberle, A., Klingbeil, D., & Schicker, J. (2000). The calculation of dynamic J_R-curves from the finite element analysis of a Charpy test using a rate-dependent damage model. *Nuclear Engineering and Design*,*198*(1), 75-87.

28. Altenhof, W., Raczy, A., Laframboise, M., Loscher, J., & Alpas, A. (2004). Numerical simulation of AM50A magnesium alloy under large deformation.*International journal of impact engineering*, *30*(2), 117-142.

29. Mediavilla, J., Peerlings, R. H. J., & Geers, M. G. D. (2006). A nonlocal triaxiality-dependent ductile damage model for finite strain plasticity. *Computer Methods in Applied Mechanics and Engineering*, *195*(33), 4617-4634.

30. Hamelin, C. J., Diak, B. J., & Pilkey, A. K. (2011). Multiscale modelling of the induced plastic anisotropy in bcc metals. *International Journal of Plasticity*,*27*(8), 1185-1202.

31. Knezevic, M., McCabe, R. J., Lebensohn, R. A., Tomé, C. N., Liu, C., Lovato, M. L., & Mihaila, B. (2013). Integration of self-consistent polycrystal plasticity with dislocation density based hardening laws within an implicit finite element framework: Application to low-symmetry metals. *Journal of the Mechanics and Physics of Solids*, *61*(10), 2034-2046.

32. Swanson Analysis Systems Inc. ANSYS, Revision 15.

33. Bao, Y., & Wierzbicki, T. (2005). On the cut-off value of negative triaxiality for fracture. *Engineering fracture mechanics*, *72*(7), 1049-1069.

34. Anderson, D., Winkler, S., Bardelcik, A., & Worswick, M. J. (2014). Influence of stress triaxiality and strain rate on the failure behavior of a dual-phase DP780 steel. *Materials & Design*, *60*, 198-207.

35. Toker, S. M., Canadinc, D., Taube, A., Gerstein, G., & Maier, H. J. (2014). On the role of slip–twin interactions on the impact behavior of high-manganese austenitic steels. *Materials Science and Engineering: A*, *593*, 120-126.

36. Lee, W. S., & Chen, T. H. (2002). Plastic deformation and fracture characteristics of Hadfield steel subjected to high-velocity impact loading. *Proceedings of the Institution of Mechanical Engineers, Part C: Journal of Mechanical Engineering Science*, *216*(10), 971-982.

37. Yang, E. E. (2010). The Effect of Carbon Content on the Mechanical Properties and Microstructural Evolution of Fe-22Mn-C TWIP/TRIP Steels.

38. http://www.dynasupport.com/howtos/element/hourglass

39. Onal, O., Bal, B., Toker, S., Mirzajanzadeh, M., Canadinc, D., & Maier, H. J. (2014). Microstructure-based modeling of the impact response of a biomedical niobium–zirconium alloy. *Journal of Materials Research*, *29*(10), 1123-1134.

40. Canadinc, D., Sehitoglu, H., Maier, H. J., & Chumlyakov, Y. I. (2005). Strain hardening behavior of aluminum alloyed Hadfield steel single crystals. *Acta materialia*, *53*(6), 1831-1842.

41. Canadinc, D., Biyikli, E., Niendorf, T., & Maier, H. J. (2011). Experimental and numerical investigation of the role of grain boundary misorientation angle on the dislocation–grain boundary interactions. *Advanced Engineering Materials*,13(4), 281-287.

42. Canadinc, D., Sehitoglu, H., Maier, H. J., & Kurath, P. (2008). On the incorporation of length scales associated with pearlitic and bainitic microstructures into a visco-plastic self-consistent model. *Materials Science and Engineering: A*, *485*(1), 258-271.

43. Kocks, U. F., Tome, C. N., & Wenk, H. R. (1998). Texture and Anisotropy. Preferred Orientations in Polycrystals and Their Effect on Material Properties. *Cambridge University, Cambridge*.

Chapter 3

A NOVEL APPROACH FOR MONITORING PLASTIC FLOW LOCALIZATION DURING SMALL-SCALE TESTING

3.1. INTRODUCTION

Ductile failure of polycrystalline materials commonly follows localization of plastic flow upon void nucleation, growth and coalescence [1,2]. However, experimental detection of each phase is highly demanding and has just very recently become practical with the aid of in-situ techniques, such as X-ray tomography [2-3]. Yet, execution of such experimentations is difficult due to delicate sample preparation requirements [4], in addition to being expensive, and thus, a number of successful continuum models have been suggested [2,6-14] for prediction of the ductile failure. In particular, a comprehensive knowledge about the role of void initiation, growth and their coalescence on plastic localization in metallic materials has emerged over the past 50 years. However, despite the large volume of numerical and analytical studies relating ductile failure to microstructural features, an adequate experimental investigation of the plastic flow localization has not been forwarded yet.

Recent developments in the field of digital image correlation (DIC) technique has enabled researchers to move towards small scale in-situ SEM tensile experiments with the aim of extending the existing knowledge on damage nucleation at the macroscopic level further down to the grain level [15-17]. While these works could not clearly demonstrate that there is a correlation between strain localization and Schmid factor within the grains [15], later it was became evident that SEM-DIC measurements used for in-situ SEM testing may have involved significant strain measurement errors [18]. The local information of strain

localization obtained in these works was restricted to the specific regions on the surface of material, hence neglecting the influence of the plastic flow localization on the overall deformation and damage initiation. In order to explore the regions beyond the specimen surface during the recent investigations of void growth mechanisms and coalescence, X-ray tomography [4-6] and synchrotron radiation laminography [3] have proven to be useful. Nonetheless, these methods are very complicated, expensive and experimentally demanding. Furthermore, their execution needs model materials which do not have realistic void geometry and distribution, and the lack of prior knowledge of the possible damage initiation sites restricts the gage length to about only 100 microns.

While the aforementioned methods can be employed for evaluation of the proposed theoretical and computational studies, their applications involve variety of assumptions and simplifications that may shadow the influence of real parameters, such as inhomogeneous structure of polycrystalline solids, crystallographic orientation, grain features and their interactions on multiscale ductile damage nucleation and growth. In this study, an in-situ SEM tensile test setup was miniaturized devising novel grips to facilitate observation of the whole surface distortion in the deformation history, such that the design of the setup included features to eliminate the spatial distortion errors that exist in in-situ SEM deformation measurements. Employing a newly proposed hybrid numerical-experimental (HNE) approach, stress-strain behavior of the material was computed following the experiment in a finite element (FE) modeling framework. Primary FE simulations were utilized in order to predict the stiffness of the inner parts of the testing machine in order to eliminate the error in the recorded displacement. Data points on the force-elongation plot were then compared with the measured elongation through the SEM to verify the HNE approach. By visual tracing of the marks and surface features thorough comparison of the incrementally captured SEM images throughout the loading, locations of "no translation" were recognized and marked

during the tensile test. Emergence of the initial localization was attributed to an instant when the position of the points on the geometrical symmetry line of the specimen moved away from their stationary state, which also constitutes the limit for uniform straining of the material. Arranging each two of the incrementally taken surface SEM images in an alternate order following the appearance of uniform straining limit, plastic flow localization events were witnessed and recorded. The current results indicate both the success and the feasibility of this novel and efficient visual method to capture the primary plastic flow localization sites in the specimen prior to necking and final failure.

3.2. EXPERIMENTAL METHOD

3.2.1. Materials and sample preparation

Dog-bone shaped tensile samples with rectangular cross sections (1 mm × 0.8 mm) and 3 mm gauge length (Fig. 3.1) were extracted from bulk austenitic stainless steel (X2 CrNiMo 18 14 3, or AISI 316L from Thyssen) using electric discharge machining (EDM). The bulk material was annealed for 5 h at 1050 ^{o}C and water-quenched prior to EDM. Young modulus and yield strength of the bulk material were measured as 210 GPa and 280 MPa, respectively. The surfaces of samples were subjected to several steps of mechanical grounding and electro-polishing with a mixture of 500 ml ethanol, 7.5 ml nitric acid and 25 ml perchloric acid (or Struers A2 electrolyte), and at 0 ^{o}C under a voltage of 55–60 V for 30 s in few intervals. Following the grounding and polishing, the thickness (t) and the width of the samples were reduced by about 0.06 – 0.12 mm and 0.1 mm, respectively.

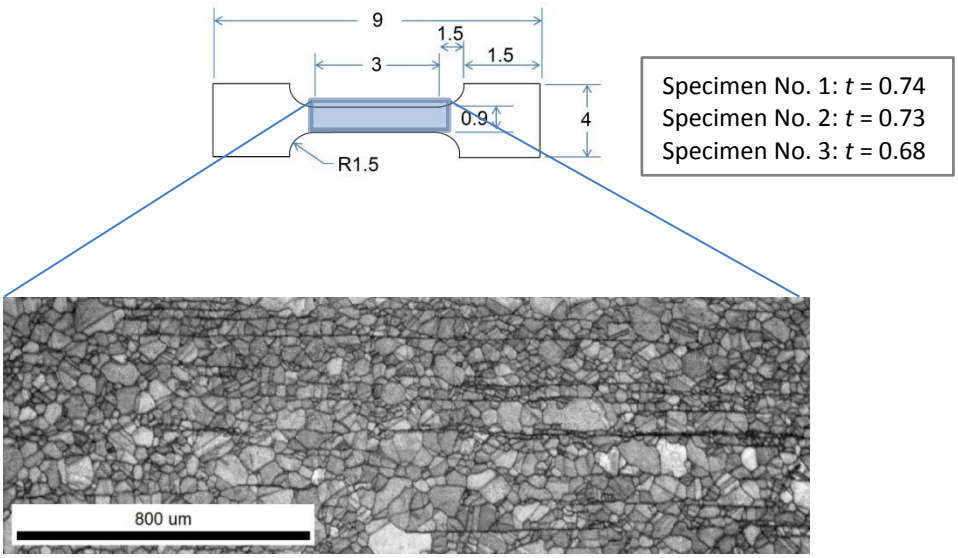

Fig. 3.1. Geometry of the dog-bone tensile test samples (respective dimensions are not drawn to the scale): all dimensions are in millimeter.

3.2.2. Test setup

In order to investigate the localization at the grain level, it is necessary to reduce the sample dimensions, such that the whole gage section can be inspected all at once. Nevertheless, a reasonable number of grains should be retained in order to observe true polycrystalline deformation behavior, and to avoid boundary condition and size effects on the material's response and damage initiation. Despite the fact that majority of previous studies have focused on localization and ductile fracture under high triaxiality conditions (e.g. notched samples), samples without notches were preferred here to avoid undesired contribution of the geometrical parameters to the ductile failure. One should also note that it is quite difficult to clamp extremely small test samples without causing damage, and the accurate manufacturing of the miniature grips can also be very challenging. Given the aforementioned limits and considerations, dimensions of dog-bone samples and grips were chosen (see Figs. 3.1 and 3.2), such that 79 grains along the gage length, 23 grains along the width and 18 grains along the thickness of the samples were obtained for an average grain size of about λ_{grain} = 38μm.

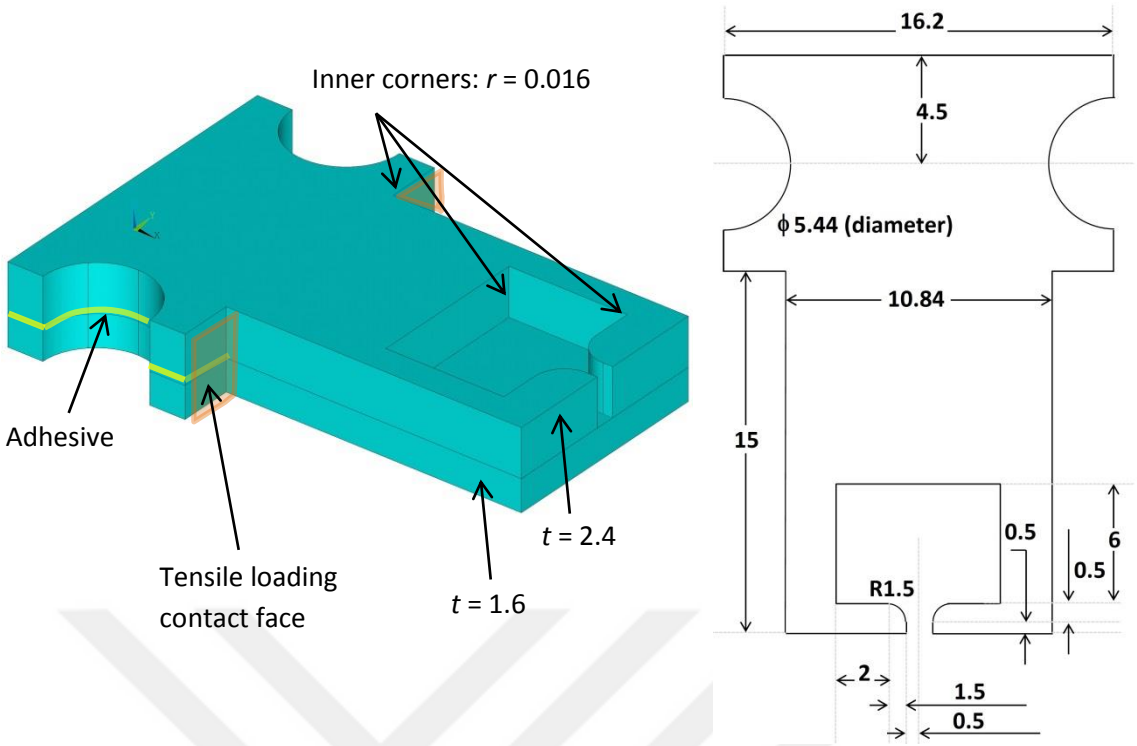

Fig. 3.2. Geometry of the designed grips for tensile deformation experiments: all dimensions are in millimeters.

Spatial and temporal distortions during the in-situ SEM experiments are the main sources of error in displacement measurements through SEM-DIC techniques [17]. Thickness reduction is one of the spatial distortions in the in-situ SEM tensile test and should be one of the main origins for inaccurate strain and displacement measurements. To address this issue in the current work, dimensions of the test setup were carefully chosen to produce an upward deflection equal to then thickness reduction in sample. Therefore, the test samples were mounted on the grips in an eccentric manner with respect to the thickness (see Fig. 3.4). The special geometry of the grips allows bending of the heads upward which causes movement of the sample in the *Z*-direction, hence eliminating the thickness reduction effect substantially – the specimen surface displacement varies between Δz = -1µm (at 50% elongation) and -9µm (at 90% elongation) in the experiment for specimen No. 3. Fig. 3.3 highlights the

aforementioned fact about the design showing deflection of the specimen using elastic-plastic FE model: details of the numerical analysis are discussed in the remainder of the paper.

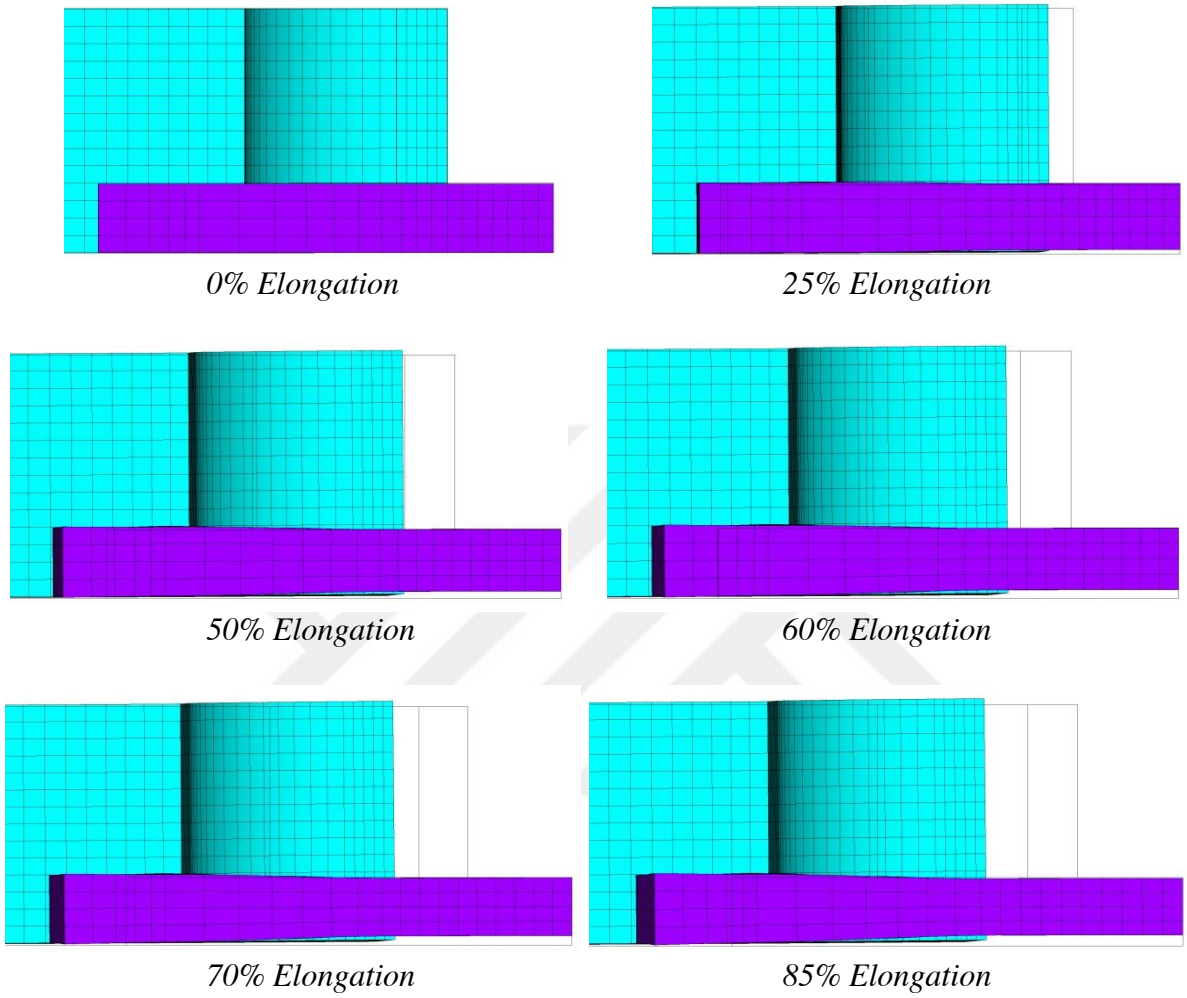

Fig. 3.3. Deflection of the fixture and sample over several stages of elongation with undeformed (original) edges from the side view, view A (see Fig. 3.6): this figure portrays the displacement of the sample in *Z*-direction, such that surface of the sample stays on its original position throughout deformation history. This is required for accurate in-situ SEM displacement measurements, specifically in large plastic deformations.

As it is seen in Fig. 3.2, each grip was made by joining two separate parts by an adhesive: the lower part was merely used for leveling the sample in its place, so it carries no load during the experiment. The grips were made from conventional maraging steel with an elastic modulus of 210 GPa and yield strength of more than 1200 MPa, and EDM was used to

machine them. In order to enhance the stiffness and yield strength of the employed maraging steel, grips were heat treated for 3 hours at 450 ^{o}C, and then the two parts of the grips were glued precisely on top of each other (see Fig. 3.2) utilizing a conventional steel adhesive in order to avoid misalignment of the sample inside the grips. Fig. 3.4 demonstrates the manufactured test samples and grips mounted on the tensile test machine.

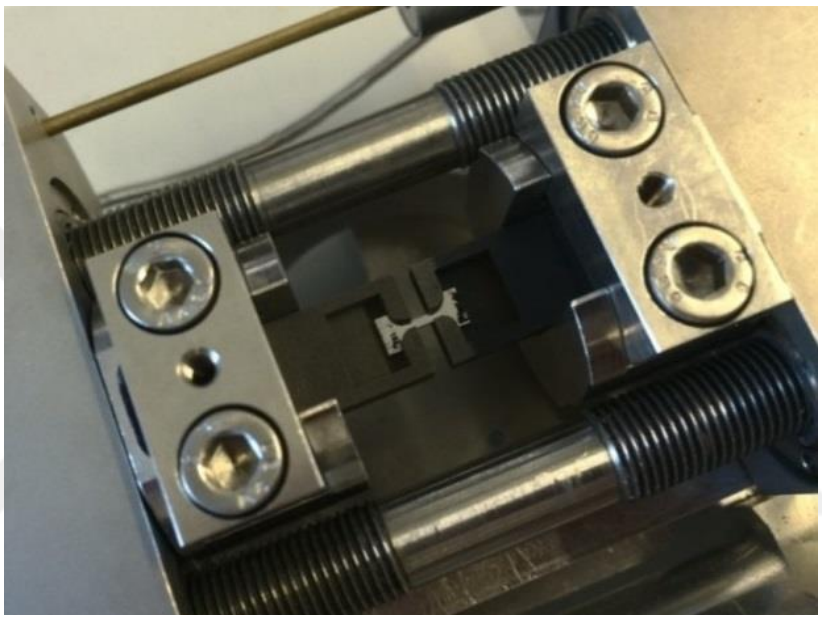

Fig. 3.4. Manufactured grips and dog-bone samples, and their mounted position on the testing device

3.2.3. In situ SEM tensile testing

Tensile test were performed at room temperature utilizing a tension/compression module of 10 kN loading stage (Kammrath & Weiss) under displacement control condition with increasing then load at a rate of 5×10^{-3} N/s inside the SEM chamber (ZEISS DSM 962) with a measurement error of 1N in force and 1-3 μm in displacement. In order to check the suitability of the designed parts and feasibility of the test, initial experiments (specimens 1 and 2) were performed outside the SEM chamber. Moreover, test setup was prepared prior to

test outside the SEM, and the samples and the grips were adjusted before transferring to the SEM chamber. Parts (specimen and grips) were fixed into their places by enhancing the force gradually up to around 1-5 N under manual control outside the SEM chamber.

Tensile tests were paused continually following the yield of the samples, in order to take the SEM images of the surface during the deformation intervals (i.e. 23 intervals with 100 μm and 200 μm elongation). The slight drops in the force deformation graph in Fig. 3.5 are the locations where the tests were paused. The recorded force-elongation curves are illustrated in Fig. 3.5: discrepancy between the graphs arises from the dissimilar cross sectional dimensions of the test samples.

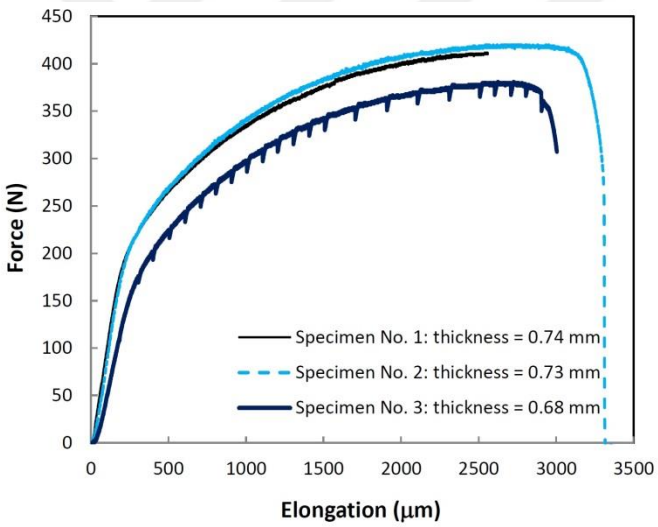

Fig. 3.5. Force-elongation behavior measured during the experiment for three samples with different thicknesses.

3.3. STRAIN MESUREMENT

3.1. Hybrid Num.-Exp. Method (HNE)

One should notice that the extreme dimensions of experimental test setup make the application of conventional methods of strain measurement, such as extensometers or strain

gages, impractical. While one alternative method can be the application of digital image correlation (DIC) technique, it is not favored in the present study owing to factors that make its utilization demanding and sometimes unreliable. For instance, finding the reliable correlation between fainting marks (i.e. scratches, grain boundaries or other surface features) as a result of large deformation in addition to new emerging symbols due to either appearance of slip system activities or annihilation of them over deformation history is still a big challenge [17-19]. Even if this challenge is overcome, it has been demonstrated [17] that using SEM images for DIC is problematic owing to the fact that during the straining the sample thickness decreases continuously, which alters the vertical distance between the electron beam gun and the surface. Therefore, computed distances on the surface reflect erratic strain values. In this study, a hybrid numerical-experimental approach (HNE) was exploited in order to find global strain values in the specimen in a more reliable and efficient manner independent of the surface dispositioning during the experiments.

First, a real-scale FE model with elastic material behavior was built to find a relationship between the error in the displacement measurement and the force using the known elastic parameters of the test material. As the linear part of the force-elongation graph obtained in the experiment represents the elastic part of material, it is possible to compute the measurement error. Then, a fully elastic-plastic FE model was established in order to compute the material response within the plastic region using the modified (corrected as error-free) force-elongation test data. In order to check the validity of the gained strains using the aforementioned technique, a visual in-situ SEM displacement measurement was also performed for several stages of loading.

3.3.2. Finite Element model

To achieve a realistic deformation of the grips (see Fig. 3.2) during the test, the whole test setup (grips and sample) should be considered in the FE model [22]. However, as the geometry of the test setup is symmetric with respect to the *X*–*Z* and the *Y*–*Z* planes (see Fig. 3.6), only a quarter of the complete structure was included in the FE simulations in order to have an optimum model size. Additionally, application of fixed boundary condition in *Z* direction ($Z = 0$) was preferred for the glued surface rather than the simulation of second part (below counterpart) of the grips to further reduce the model size.

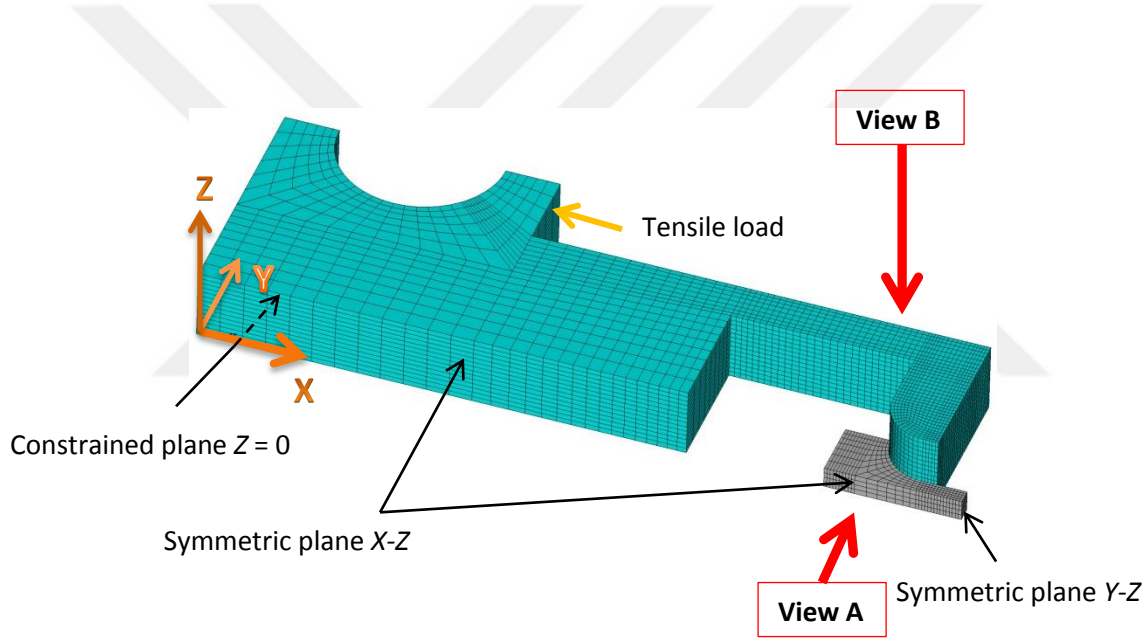

Fig. 3.6. FE model showing employed mesh density, constrains, coordinate system, and loading direction and its location on the test setup.

In order to mesh the test setup, linear isoparametric cubic SOLID185 elements were used. This 2 × 2 × 2 integration point element has 8 nodes (one node at each vertex) and each node has 3 degree of freedom displacement in *X*, *Y* and *Z* directions [23]. To include contact between the curved area of the dog-bone shaped sample and the contacted area on the grip, CONTA174 and TARGE170 were used to mesh the interfaces. These contact elements allow

for pressure to be transferred between the contacting surfaces but without penetrating each other [23]. In the model, the friction between contacting surfaces was included using the elastic Coulomb friction model with a friction coefficient of $\mu = 0.74$, which is suggested as the friction coefficient of steel and steel dry surfaces [24]. Sensitivity analysis disclosed that slight changes in the value of the friction coefficient do not considerably alter the deformation response in the FE simulation.

In the initial FE model, an elastic material behavior was considered for both materials with a Poisson's ratio of $\nu = 0.29$ and elastic modulus of $E = 210$. This FE analysis was primarily conducted using an elastic behavior for the specimen in order to check the suitability of the elastic behavior assumption for the grip material. Stress distribution results obtained in initial elastic FE model proved that the material will never go beyond the yield limit of maraging steel after heat treatment (i.e. $Sy > 1700$ MPa), so assuming an elastic behavior for the grip material should be acceptable.

To constrain the FE model, symmetric boundary conditions were applied in *X*-*Z* and *Y*-*Z* planes (see Fig. 3.6) and nodes on the bottom face of grip (adhesive region) were fixed in the *Z* direction. Nonetheless, test specimen stayed unconstrained in *Z* direction and the imposed contact condition was used for keeping the sample in place during the deformation. The FE model has the exact dimensions of the specimen No. 3 with a thickness of 0.68 mm and width of 0.9 mm. To create deformation, displacement of 1.4 mm was applied on the end of the grip (see Fig. 3.6) in –*X* direction.

3.3.3. Modification of the elongation data using FE model

The initial FE simulation results using just elastic material behavior were shown in Fig. 3.7. Apparently, the stiffness of the test setup obtained from the testing machine was smaller than its real value which can be computed using FE model. Calculation of the error in displacement measurement (Δx_e) results in finding a linear correlation between the Δx_e and force (F or F^{exp}) in the employed test conditions (constant strain rate): see Eq. 3.1-3.3.

$$\Delta x_e \propto F \tag{3.1}$$

$$\Delta x_e = h \times F \tag{3.2}$$

$$\Delta x_e = \frac{1}{K_e} \times F \tag{3.3}$$

In the above equations, h is the compliance of the test device. Modified (error-free) experimental displacement of the test setup (Δx_{setup}^{exp}) were calculated using Eqs. 3.4-3.7. In these equations total displacement measured during the test is shown by Δx_t, and stiffness of the test setup, device (attributed to error) and total (attributed to the whole stiffness of the device and test setup) are shown as K_{setup}, K_e and K_t, respectively.

$$\Delta x_t^{exp} = \Delta x_{setup}^{exp} + \Delta x_e^{exp} \tag{3.4}$$

$$\frac{F^{exp}}{K_t} = \frac{F^{exp}}{K_{setup}} + \frac{F^{exp}}{K_e} \tag{3.5}$$

$$K_e = \frac{K_{setup}^{FE}.K_t^{exp}}{K_{setup}^{FE} - K_t^{exp}} \tag{3.6}$$

$$\Delta x_{setup}^{exp} = \Delta x_t^{exp} - \frac{F^{exp}}{K_e} \tag{3.7}$$

Replacing the values in the Eq. 3.6 gives stiffness of the device (error) as K_e = 1.338 N/μm, and so real displacement of the test setup was computed. Modified data using the real

displacement of the test setup is depicted in Fig. 3.7, and compared with original data. It is assumed that the correlation between the error and force stays linear also within the inelastic region. While one way for validating this is testing a material with higher yield stress, in this study an in-situ SEM deformation measurement was carried out to show this correlation within few stages of deformation (see Fig. 3.8). Fig. 3.8 reveals that the obtained results through the application of the HNE method agree well with the in-situ SEM measurements.

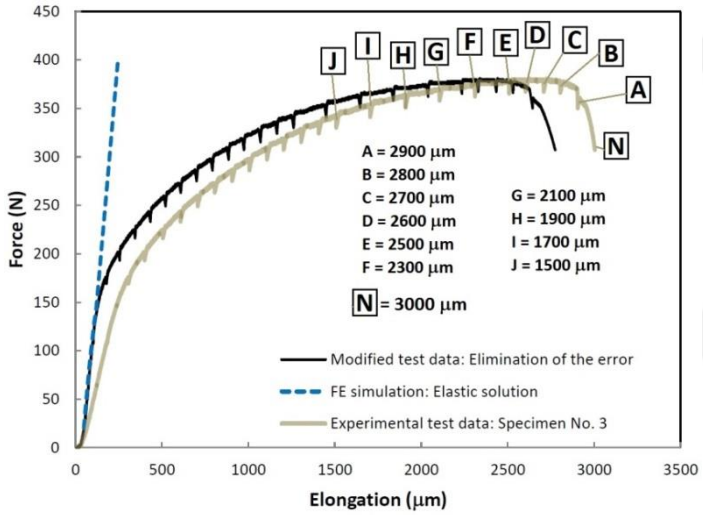

Fig. 3.7. Force-elongation behavior measured during the experiment, and compared with the elastic FE simulation and modified force-elongation curve computed in this study using FE analysis. Loading stages of interest were denominated based on the annotation provided, which will be used in the remainder of the paper.

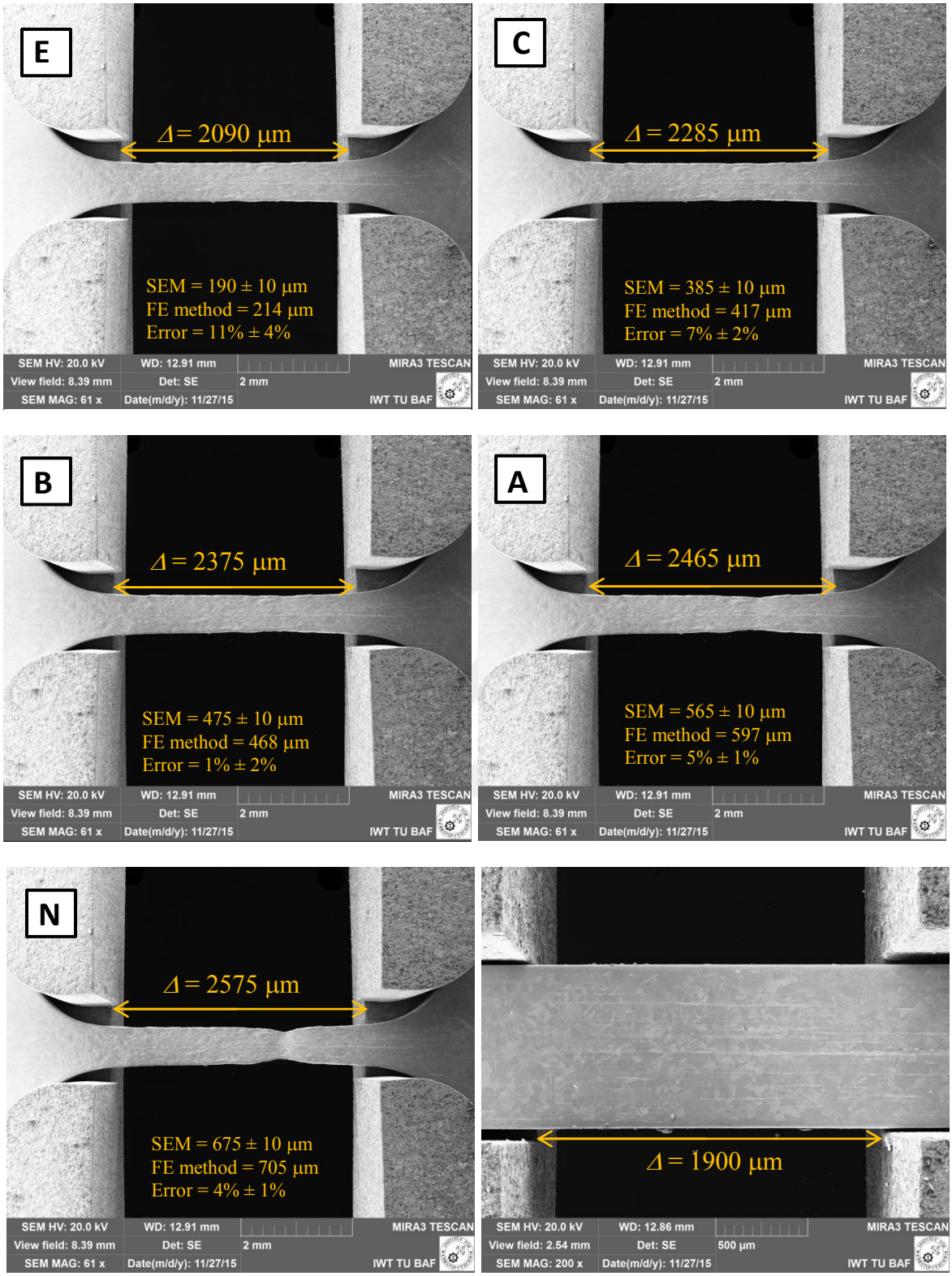

Fig. 3.8. Elongation measured using the in-situ SEM images compared with computed modified data using the FE analysis (error-free) for five last stages of the deformation prior to necking (see denomination of the stages in Fig. 3.7).

Through the application of the initial FE model, yield strength of the material was computed as about 275 MPa for specimen No. 3. Although the elimination of the error in displacement provides realistic values for the elongation of the test setup, the stiffness of the grips and specimen heads affect the elongation of the gage length of the specimen, such the elongation within the gage length cannot be calculated directly. Alternatively, the proposed HNE approach was taken into account to derive hardening behavior of the material according to the described procedure in following section.

3.3.4. Obtaining material response: numerical procedure details

FE simulation was performed using a multilinear kinematic hardening material model via ANSYS code [22] with the explained FE model parameters in previous sections. The first step of numerical analysis carried out using a bilinear material data with the tangent modulus of the elastic part as $E_{t(0)} = E = 210$ GPa and an initial value for plastic part as $E_{t(1)}$ (i.e. $E_{t(1)} =$ 10000 MPa). Then, reaction force on cross section of the specimen was computed after one step of elongation $\Delta x_1 = \Delta x_{yield} + \Delta S$ ($\Delta x_{i+1} = \Delta x_i + \Delta S$ and $i = 0,1,2, \ldots$ and $\Delta x_0 = \Delta x_{yield}$) and the magnitude of the discrepancy between this value (F^{FE}) and the forces on the modified experimental data (see Fig. 3.7) at the same elongation (F^{exp}) was calculated. The $E_{t(1)}$ was updated in the FE simulation until the discrepancy between the forces after ΔS elongation becomes less than an acceptable error, $|F^{exp} - F^{FE}| < \delta$. When the converged value of the $E_{t(i)}$ was achieved, the average strain at the cross section of the sample was computed after Δx_i elongation: This strain gives the update point for the next hardening slope (young modulus of $E_{t(i+1)}$) in the input material behavior. Repeating the explained process produced the material behavior of used in the experiment. Fig. 3.9 shows a schematic presentation of the employed numerical approach in this study.

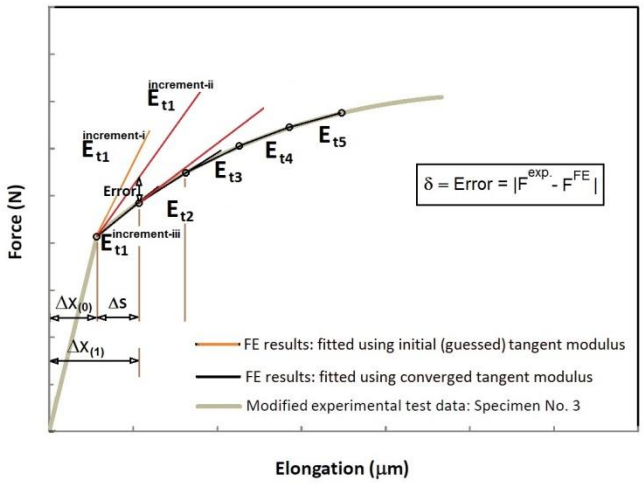

Fig. 3.9. A schematic representation of the adopted numerical approach to calculate the material response in in-elastic region.

Fig. 3.10 shows converged force-elongation results obtained through the adopted numerical approach to find material response which is shown in Fig. 3.11 as true and engineering stress-strain curves. Deformation results of the FE simulation for two stages of loading is depicted in Fig. 3.12. As deformation of the head of the specimen shows, application of the strain gages in these dimensions, if possible, would give inaccurate results for strains.

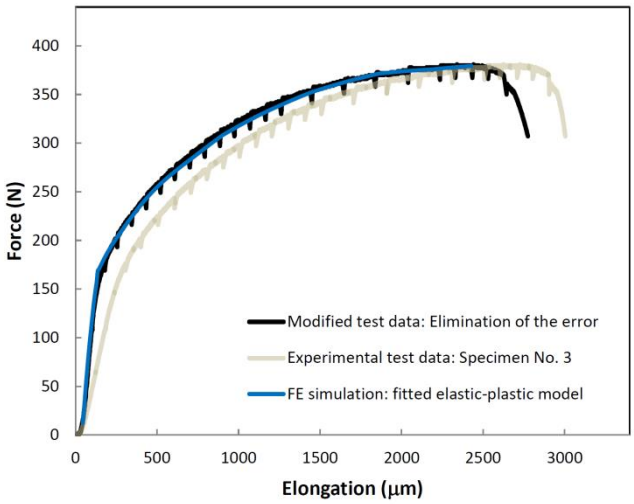

Fig. 3.10. Force-elongation behavior computed using the elastic-plastic FE model compared with the measured response during the experiment.

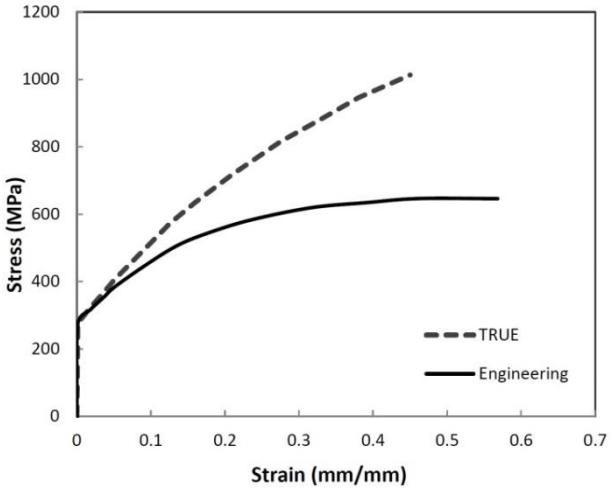

Fig. 3.11. Computed material behavior plotted as true stress-strain curve and engineering stress-strain curve using the HNE method.

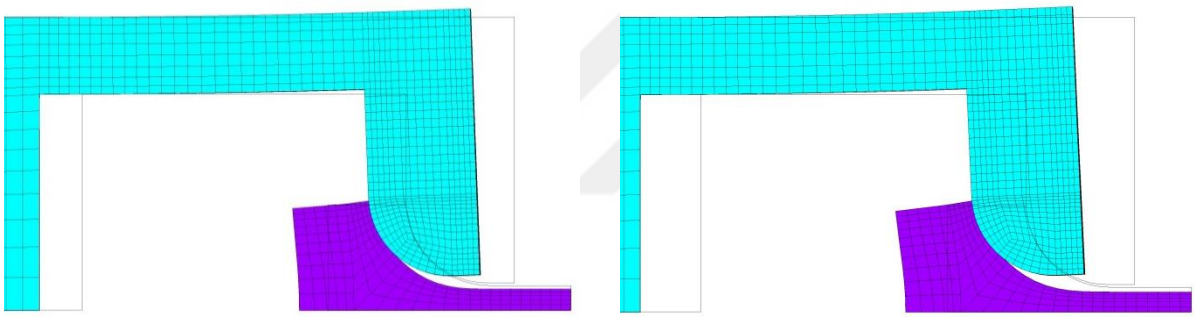

60% Elongation *85% Elongation*

Fig. 3.12. Deflection of the fixture and sample after 60% and 85% of elongation from the top view, *view B* (see Fig. 3.6).

In order to check the effect of the bending stresses on measurement readings from SEM images, we derived the bending stress values over the surface of the sample for the entire history of the deformation. As it is seen in Fig. 3.13, after the elastic deformation the magnitude of the bending stresses reduced to approximately 2 MPa and remained almost constant during the straining.

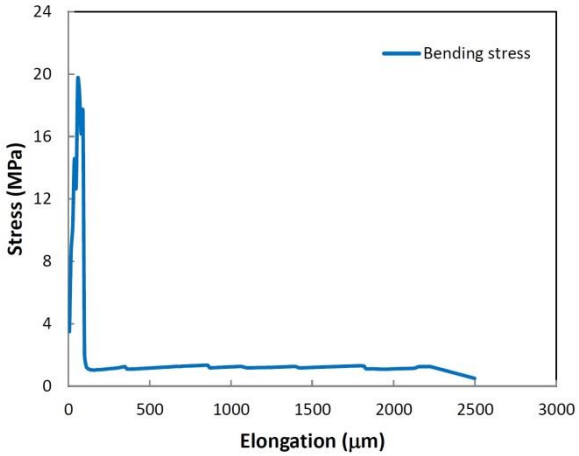

Fig. 3.13. Variation of the bending stress on the surface of the sample over the modified displacement history obtained through the FE simulation.

3.4. MACROSCOPIC LOCALIZATION: IN-SITU SEM IMAGE ANALYSIS

The new experimental method was proposed to test the material at very small dimensions for better observation of the plastic localization events at grain level and within the entire gage section. Incrementally taken SEM images were very carefully scrutinized in order to observe even the slightest displacement anomalies over the deformation history. Theoretically, using a periodic cell model including a void band between two outer blocks (without void), it has been shown that macroscopic localization can be identified during the history of the deformation when the plastic straining of the material is confined to the band and elastic unloading occurs within the two outer layers [23]. In the present study, it was assumed that macroscopic localization occurs when the uniform straining limit is reached, which will be identified with the movement of an imaginary geometrical symmetry line of the specimen pictured on the specimen in the overall straining history (see Video 3.1). While the symmetry line on the sample during the deformation specifies the location of the material points on the sample, which has zero displacement, intuitively it can be concluded that the new location of the zero displacement material points (when symmetry line moves) should indicate the bands

of the matrix material with higher volume density of damage, including voids and developed or coalesced voids. It should be noted that void coalescence and growth happen simultaneously in low traixaility ranges [2] and they cannot easily be distinguished from each other.

By arranging each pair of sequentially taken surface SEM images following the uniform straining limit in an alternate order for several repetitions (see Fig. 3.14), plastic localization regions became manifest on surface of polycrystalline metallic materials (see Video 3.2). This demonstrates feasibility of the presented method in recording the macroscopic plastic localization during the tensile experiment using microscale in-situ SEM tensile testing. Fig. 3.14 shows inverse pole figure of the test sample (in loading direction) prior to test mapped on the SEM image pointing couple of macroscopic localizations (i.e. second and the forth) observed during the test and final necking site.

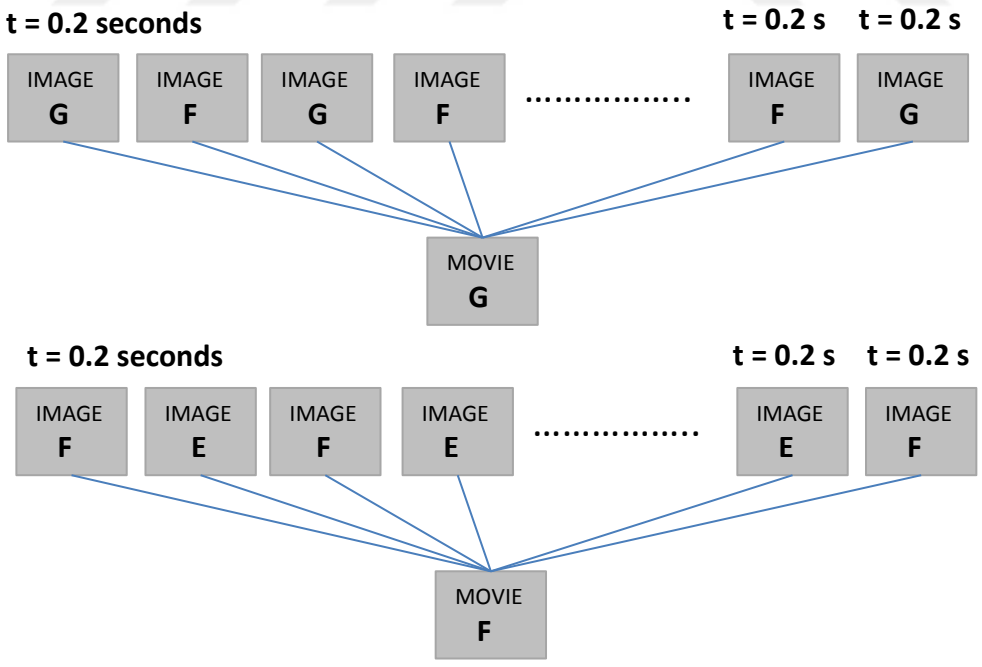

Fig. 3.14. The employed approach for making movies that reveals macroscopic localization locations.

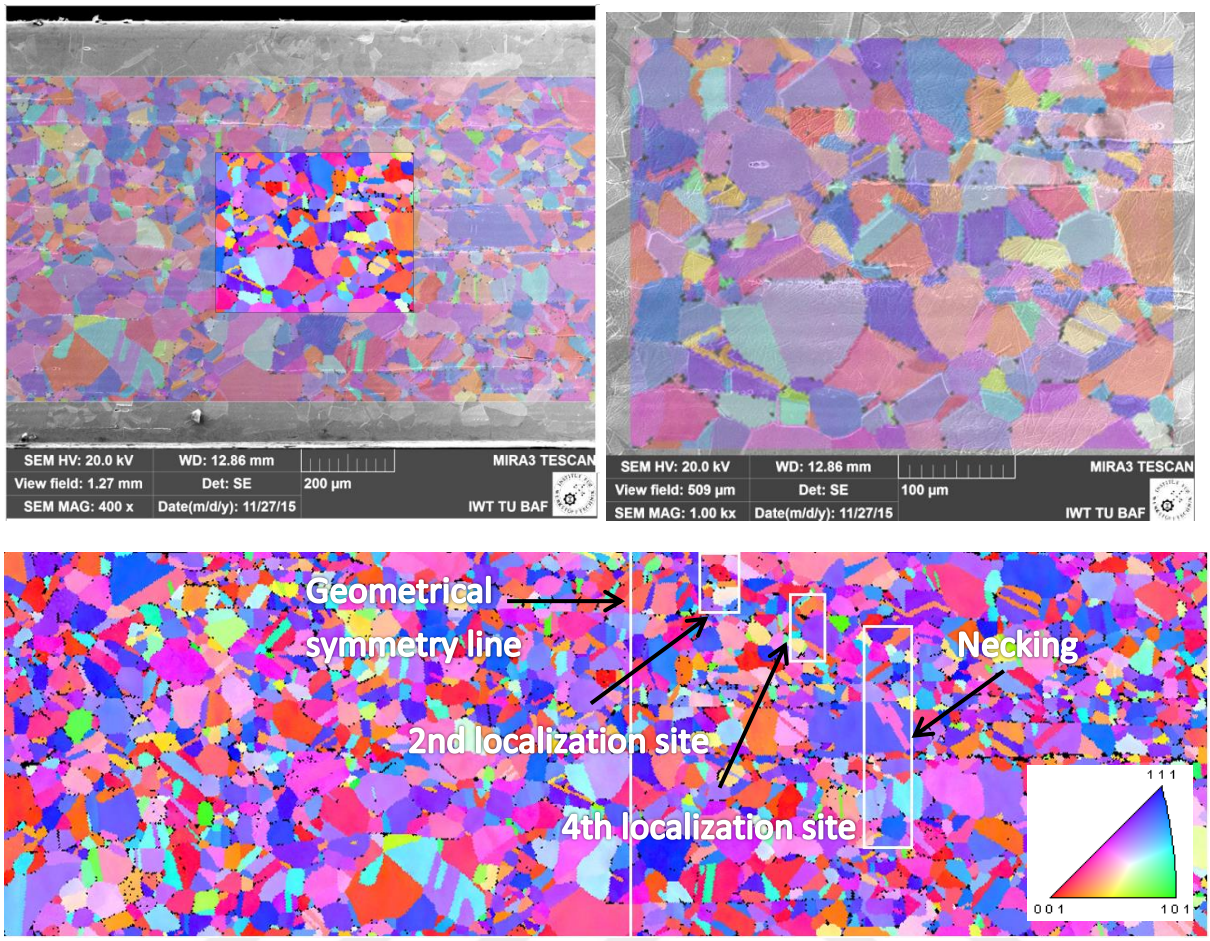

Fig. 3.15. Microstructure of the AISI 316L SS microstructure showing the regions of plastic flow localizations, and the corresponding inverse pole figure (IPF) map.

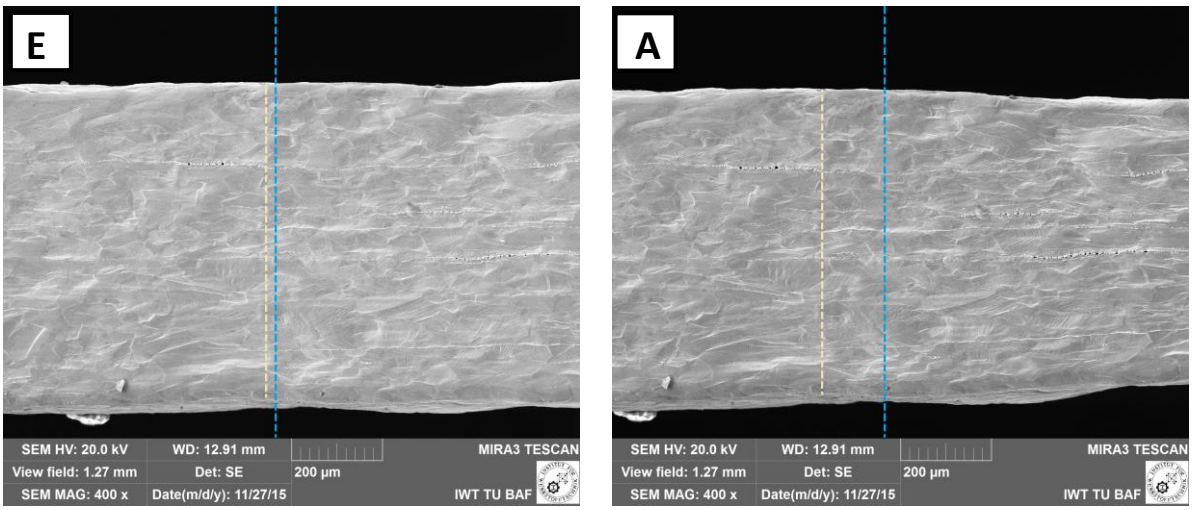

Video. 3.1. Deformation of the tensile test sample over the whole elongation history, showing the instant when the uniform straining limit reaches (with movement of the symmetry line of the loading): appearance of the yellow dashed line in the video signals the end of the uniform straining limit.

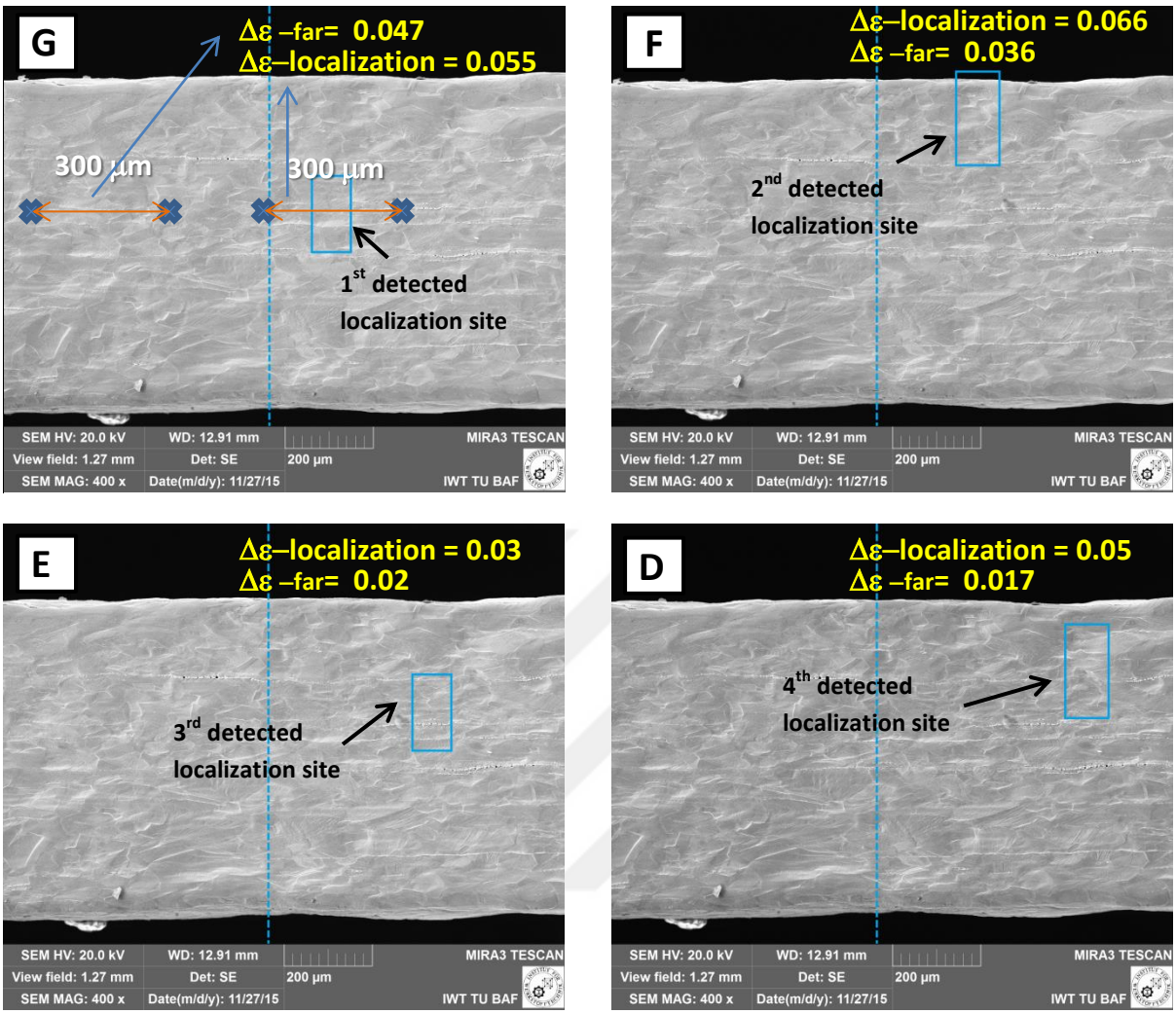

Video. 3.2. Observation of the plastic flow localization is captured in the boxes: these are attributed to the location of the material points which have no movement during the two successive loading stages. Four videos disclose the macroscopic localization event for the experimentally measured elongation of 2100, 2300, 2500 and 2600 µm displacement – for illustrated points of G-F, F-E, E-D and D-C in Fig 3.7, respectively.

3.5. CONCLUSIONS

Ductile failure of polycrystalline materials is commonly followed by localization mechanisms stems from void nucleation, growth and coalescence. However, experimental detection of it

at grain scale is not straightforward task since failure normally begins from inside the material. This study initially introduces a novel small scale experimental method for obtaining the material response using a numerical method. Later, this new testing method was utilized for observing the macroscopic localization. Results clearly certify the correctness of the deployed measurement technique in the presented work. Following concluding points highlights findings of the current research:

- Developed *testing setup* introduces a novel simple approach for tensile testing of the small scale solids to eliminate vertical spatial distortions error involved in in-situ SEM displacement/strain measurement methods.
- Proposed tensile testing procedure is a capable way toward testing extreme dimensions of the metallic materials where size restrictions prevent application of the traditional methods of strain measurement.
- It is shown that measurement error of the employed miniature tensile testing machines can be calculated and calibrated to give realistic values of deformations without the aid of other techniques of strain measurement. And if combined with the proposed HNE method, global strain values should be extracted correctly.
- It is illustrated that observation of plastic flow localization initiation sites and its development during the deformation history without the aid of computational analysis in real polycrystalline metallic materials is feasible with merely use of in-situ SEM images.
- Beginning of the plastic localization can be attributed to the instant when the geometrical symmetry line (i.e. the location of the material points with zero displacement during the deformation history) moves away from its original state: this is the limit for uniform straining capacity of polycrystalline material.
- Recorded experimental test results demonstrates that beginning of ductile damage does not restricted to a specific location causing the rupture of the sample at that site, rather damage initiates in different parts of the sample in history of deformation and it either further develops or seizes while new localization sites emerges with higher volume fraction of voids/damage which are more suitable places for damage evolution.

3.6. ACKNOWLEDGEMENTS

Financial supports by Koç University Graduate School of Sciences and Engineering, and Institute of Materials Engineering, Technische Universität Bergakademie Freiberg, Freiberg, Germany, are gratefully acknowledged.

BIBLIOGRAPHY

1. Rogers, H. C. (1960). The tensile fracture of ductile metals. *AIME trans*,*218*(3), 498-506.
2. Tekoğlu, C., Hutchinson, J. W., & Pardoen, T. (2015). On localization and void coalescence as a precursor to ductile fracture. *Philosophical Transactions of the Royal Society of London A: Mathematical, Physical and Engineering Sciences*, *373*(2038), 20140121.
3. Morgeneyer, T. F., Helfen, L., Mubarak, H., & Hild, F. (2013). 3D digital volume correlation of synchrotron radiation laminography images of ductile crack initiation: an initial feasibility study. *Experimental Mechanics*, *53*(4), 543-556.
4. Hosokawa, A., Wilkinson, D. S., Kang, J., & Maire, E. (2013). Onset of void coalescence in uniaxial tension studied by continuous X-ray tomography. *Acta Materialia*, *61*(4), 1021-1036.
5. Lecarme, L., Maire, E., KC, A. K., De Vleeschouwer, C., Jacques, L., Simar, A., & Pardoen, T. (2014). Heterogenous void growth revealed by in situ 3-D X-ray microtomography using automatic cavity tracking. *Acta Materialia*, *63*, 130-139.
6. Weck, A., Wilkinson, D. S., & Maire, E. (2008). Observation of void nucleation, growth and coalescence in a model metal matrix composite using X-ray tomography. *Materials Science and Engineering: A*, *488*(1), 435-445.
7. Rice, J. R. (1976). *The localization of plastic deformation* (pp. 207-220). Division of Engineering, Brown University.
8. Tvergaard, V. (1982). On localization in ductile materials containing spherical voids. *International Journal of Fracture*, *18*(4), 237-252.
9. Pardoen, T., & Hutchinson, J. W. (2000). An extended model for void growth and coalescence. *Journal of the Mechanics and Physics of Solids*, *48*(12), 2467-2512.
10. Benzerga, A. A., & Leblond, J. B. (2010). Ductile fracture by void growth to coalescence. *Advances in Applied Mechanics*, *44*, 169-305.
11. Ruggieri, C. (2004). Numerical investigation of constraint effects on ductile fracture in tensile specimens. *Journal of the Brazilian Society of Mechanical Sciences and Engineering*, *26*(2), 190-199.
12. Morin, L., Leblond, J. B., & Tvergaard, V. (2016). Application of a model of plastic porous materials including void shape effects to the prediction of ductile failure under shear-dominated loadings. *Journal of the Mechanics and Physics of Solids*, *94*, 148-166.

13. Jiang, W., Li, Y., & Su, J. (2016). Modified GTN model for a broad range of stress states and application to ductile fracture. *European Journal of Mechanics-A/Solids*, *57*, 132-148.

14. Mirzajanzadeh, M., & Canadinc, D. (2016). A Microstructure-Sensitive Model for Simulating the Impact Response of a High-Manganese Austenitic Steel. *Journal of Engineering Materials and Technology*, *138*(4), 041004.

15. Tschopp, M. A., Bartha, B. B., Porter, W. J., Murray, P. T., & Fairchild, S. B. (2009). Microstructure-dependent local strain behavior in polycrystals through in-situ scanning electron microscope tensile experiments. *Metallurgical and Materials Transactions A*, *40*(10), 2363-2368.

16. Walley, J. L., Wheeler, R., Uchic, M. D., & Mills, M. J. (2012). In-situ mechanical testing for characterizing strain localization during deformation at elevated temperatures. *Experimental mechanics*, *52*(4), 405-416.

17. Papasidero, J., Doquet, V., & Lepeer, S. (2014). Multiscale investigation of ductile fracture mechanisms and strain localization under shear loading in 2024-T351 aluminum alloy and 36NiCrMo16 steel. *Materials Science and Engineering: A*, *610*, 203-219.

18. Kammers, A. D., & Daly, S. (2013). Digital image correlation under scanning electron microscopy: methodology and validation. *Experimental Mechanics*,*53*(9), 1743-1761.

19. LePage, W. S., Daly, S. H., & Shaw, J. A. (2016). Cross Polarization for Improved Digital Image Correlation. *Experimental Mechanics*, 1-17.

20. Kammers, A. D., & Daly, S. (2013). Self-assembled nanoparticle surface patterning for improved digital image correlation in a scanning electron microscope. *Experimental Mechanics*, *53*(8), 1333-1341.

21. Self-Assembled Nanoparticle Surface Patterning for Improved Digital Image Correlation in a Scanning Electron Microscope

22. Swanson Analysis Systems Inc. ANSYS, Revision 15.

23. Swanson Analysis Systems Inc, 2007. ANSYS, Release 15. Contact Technology Guide. Swanson Analysis Systems Inc (Chapter 3). Surface-to-Surface Contact.

24. Online: http://www.physlink.com/Reference/FrictionCoefficients.cfm, web site of Physlink.com containing coefficients of static and kinetic friction.